Pertanika Journal of SCIENCE & TECHNOLOGY
VOLUME 15 NO. 2 (JULY 2007)

Collapsibility and Volume Change Behavior of Unsaturated Residual Soil

Bujang B.K. Huat[1], Faisal Hj. Ali[2] and Choong Foong Heng[2]
[1]Department of Civil Engineering, Universiti Putra Malaysia,
43400 UPM, Serdang, Selangor, Malaysia
[2]Department of Civil Engineering, University of Malaya,
Kuala Lumpur, Malaysia

ABSTRACT

Residual soils occur in most countries of the world but the greater areas and depths are normally found in tropical humid areas. In these places, the soil forming processes are still very active and the weathering is much faster than the erosive factor. Most residual exhibit high soil suctions for most of the year. The absence of positive pore water pressure except immediately after rain, renders conventional soil mechanics for saturated soil irrelevant. In particular, the effective stress theories of saturated soil are not applicable at the practical level. Ignorance or lack of understanding of the geotechnical behavior of soil in the partially or unsaturated state has caused a lot of damages to infrastructures, buildings and other structures. For instances, the collapsibility and volume change of partially saturated soils in connection with the drying or wetting causes a lot of damage to foundation, roads and other structures. As such, the development of extended soil mechanics, which embraces the soil in the unsaturated state or subjected to soil suction, is essential. This paper examines the collapsibility and volume change behavior specifically of an unsaturated residual soil under various levels of applied matric suction $(u_a - u_w)$, and net mean stress $(\sigma - u_a)$ in a predetermined stress path. The volume change of the soil is found to be sensitive to both the applied matric suction and net mean stress. The soil is found to exhibit a collapsibility behavior upon a reduction in applied matric suction to 25 kPa at constant net mean stress.

Keywords: Collapsibility, matric suction, residual soil, void ratio, volume change

INTRODUCTION

Residual soils occur in most countries of the world but the greater areas and depths are normally found in tropical humid areas. In these places, the residual soil (also known as tropical residual soils) forming processes are still very active and their development due to weathering is much faster than the erosive factor. The origin, formation and occurrence of tropical residual soils have been described in detail by Singh and Huat (2004).

A deep groundwater condition is not unusual in tropical residual soils especially within steep slopes. Soil above the groundwater is certainly unsaturated, hence negative pore water pressure also known as matric suction plays an important role in controlling the shear strength and consequently the stability of many steep slopes.

Most residual exhibit high soil suctions for most of the year. The absence of positive pore water pressure except immediately after rain, renders conventional soil mechanics for saturated soil irrelevant. In particular, the effective stress theories of saturated soil are not applicable at the practical level.

Ignorance or lack of understanding of the geotechnical behavior of soil in the partially or unsaturated state has caused a lot of damages to infrastructures, buildings and other structures. For instances, the collapsibility and volume change of partially saturated soils in connection with the drying or wetting causes a lot of damage to foundation, roads and other structures. As such, the development of extended soil mechanics to embrace soil in the unsaturated state or subjected to soil suction is essential.

As the name suggest, unsaturated soil means soil that is not fully saturated i.e. soil which contains both air and water phases within its soils phase. However, in contrast with Bishop's (1959) concept of unsaturated soil, it is accepted that the state of stress in the water phase rather than the degree of saturation should be used (Fredlund and Morgenstern, 1976, 1977; Fredlund and Rahardjo, 1993).

The two stress state variables most commonly used are the net normal stress, $(\sigma - u_a)$, and the matric suction, $(u_a - u_w)$, which is found to be the most satisfactory for engineering purposes (Fredlund and Morgenstern, 1976, 1977; Fredlund et al. 1978, Fredlund, 1979; Fredlund and Rahardjo 1993; Fredlund et al., 1978). This combination has the advantage of only one stress state variable is affected when the pore water pressure is changed. Or, in other words, effects of change in total normal stress can be separated from the effects caused by a change in the pore water pressure.

Numerous researches have studied the volume change behavior of partially saturated soil, i.e. the swelling or collapsing behavior of soil upon wetting, or reduction in suction. Examples are given by El-Sohby and Rabbaa (1984), El-Sohby and Elleboudy (1987), Lawton et al. (1989), Tadepalli and Fredlund (1991), Sharma and Wheeler (2000), Chiu and Ng (2003) and Wheeler et al. (2003). This paper examines the collapsibility and volumes change behavior specifically of an unsaturated residual soil under various levels of applied matric suction $(u_a - u_w)$, and net mean stress $(\sigma - u_a)$ in a predetermined stress path.

EXPERIMENTAL SET-UP

The conventional experimental set-up for the testing of fully saturated soil is not suitable to be used for the testing of unsaturated soil. In view of this, a special experimental set-up has been developed in order to perform the test program described in this paper. With the specially developed experimental set-up, unsaturated soil can be tested with various levels of applied matric suction and net mean stress in a predetermined stress path. Both the overall (structural) volume change and water volume change of the soil sample can be monitored the tests are performed.

In this study, a series of suction controlled isotropic compression tests are performed to determine the collapsibility and volume change of the unsaturated residual soil.

Fig. 1 shows a schematic diagram of the experimental set-up. The test panel consists of a double-walled cell, volume change indicators, diffused air volume indicators, pressure application system, pressure transducers and pressure gauges. The results of the test were monitored and recorded by a data logger connected to a personal computer.

The suction was applied by means of axis-translation technique to avoid cavitations (Hilf, 1956). In this technique, the air pressure (P_a) and back water pressure (P_w) were applied on the soil sample. The difference between the air pressure (P_a) and the back water pressure (P_w) applied on the sample is taken as the applied matric suction $(P_a - P_w)$. In this study, the air pressure was applied to the top of the sample whereas the back water pressure was applied to bottom of the soil sample. The matric suction applied is not to exceed the air entry value of the high air entry ceramic disc at the pedestal of the cell.
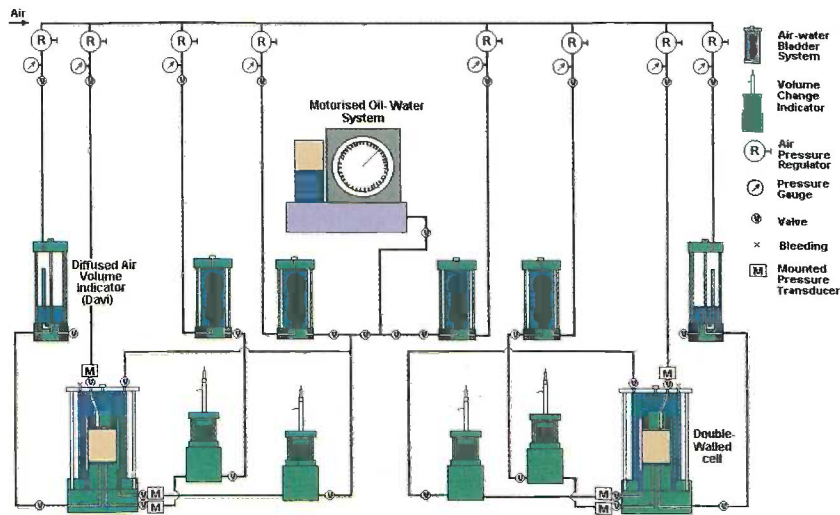
Fig. 1: Schematic diagram of the experimental set-up

Net mean stress applied to the samples in the study is taken as P-P_a where P is the all round cell pressure applied to the soil sample and P_a is the air pressure applied to the top of the sample. The back water pressure was applied through an air/water bladder system, and monitored by means of a pressure transducer. Another set of air/water bladder system with the similar design was used for the application of cell pressure. The Wykeham Ferrance constant pressure unit (motorized oil water system) is also used when the pressure applied exceeded 500 kPa.

The structural (overall) volume change and water phase volume change are measured by means of automatic volume change indicators. The pressure and volume change measured by the pressure transducers and volume change indicators were recorded by means of a data logger, which are then retrieved by a personal computer.

In order to ensure that the triaxial cell does not experience significant volume change when the pressure is altered, a double-walled cell was specially designed and fabricated.

For soil sample, disturbed soils was obtained from a cut slope at KM 31 along the Karak-Kuala Lumpur Highway, Malaysia. The soil was residual soil of weathering grade VI, based on the commonly used classification of Little (1969), and McLean and Gribble (1979), as shown in Table 1. The soil had formed over commonly found porphyritic biotite granite bedrock of Peninsular Malaysia (Raj, 1985).

The soil sample was obtained from about 3 to 4 meters below the ground surface by means of auger. Table 2 summarizes the basic properties of the soil samples, which can be described as yellowish brown sandy clay. The soil sample was first air dried in the laboratory at room temperature for about 2 weeks, as lumps broken down by means of a rubber hammer. The air-dried soil was then carefully and thoroughly mixed with a predetermined amount of distilled water, approximately 20%, which is close to the optimum moisture content obtained from the standard proctor compaction test. Static compaction is then carried out to mould the sample to ensure a homogeneous and identical sample. A similar compaction method has been applied by Booth (1975) and Nagaraj and Murthy (1985).

Bujang B. K. Huat, Faisal Hj. Ali and Choong Foong Heng

TABLE 1
Classification of the weathering profile (McLean and Gribble, 1979)

Weathering classification		Description
Term	Grade	
Residual soil	VI	All rock material is converted to soil; the mass structure and material fabric are destroyed; there is a large change in volume but the soil has not been significantly transported.
Completely Weathered	V	All rock material is decomposed and/or disintegrated to soil; the original mass structure is still largely intact.
Highly Weathered	IV	More than half of the rock material is decomposed and/or disintegrated to soil; fresh or discolored rock is present either as a discontinuous framework or as core stones
Moderately Weathered	III	Less than half of the rock material is decomposed and/or disintegrated to soil; fresh or discolored rock is present either as a discontinuous framework or as core stones
Slightly Weathered	II	Discoloration indicates weathering of rock material and discontinuity surfaces; weathering may discolor all the rock material.
Fresh Rock	I	No visible sign of rock material weathering; perhaps slight discoloration on major discontinuity surfaces

TABLE 2
Basic properties of the residual soil sample

Liquid limit	98%
Plastic limit	49%
Optimum moisture content	19.5%
Maximum dry density	1.52 Mg/m^3
pecific gravity	2.7
Sand content	45%
Silt content	15%
Clay content	40%
Type of clay mineral (X-ray diffraction)	Kaolinite

TEST PROGRAM

The main objective of the study was to investigate the collapsibility and volume change behavior of a granitic residual soil when subjected to various levels of matric suction ($u_a - u_w$) and net mean stress ($\sigma - u_a$) in predetermined stress paths. The stress paths chosen are shown in *Fig. 2* and Table 3. Six statically compacted samples were tested, designated as S1, S2, S3, S4, S5 and S6. Note that all the samples were subjected to preset matric suction throughout the test, except for samples S1.

For samples subjected to the matric suction, the air pressure applied to the samples was kept at 300 kPa level throughout the test. The changes in the matric suction and net mean stress were performed by varying the back water pressure and cell pressure respectively. For sample not subjected to the matric suction, the net mean stress was changed by varying the cell pressure whilst keeping the back water pressure at 300 kPa throughout the test.
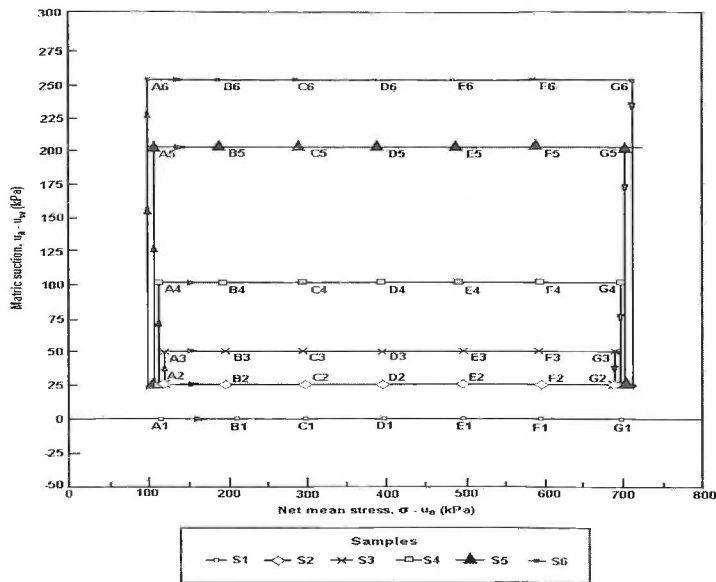
88

Pertanika J. Sci. & Technol. Vol. 15 No. 2, 2007

Fig. 2: Stress paths of samples tested

TEST RESULTS AND DISCUSSION

The plot of void ratio of the samples at various stress points versus the net mean stress is shown in *Fig. 3*. The net mean stresses are plotted both in normal and log scale.

For sample S1 which was not subjected to any matric suction throughout the test, the void ratio of the sample was found to decrease significantly as the net mean stress was elevated to higher levels in stress paths A1→ B1, B1→ C1, C1→ D1, D1→ E1, E1→ F1 and F1→G1, as shown in *Fig. 3*.

For the samples subjected to matric suction, the void ratio of the samples decreased when the applied matric suction was increased to the higher levels at net mean stress of 100kPa. Similar report on the decrease in void ratio or volume of soil with an increase in matric suction has also been made by Josa *et al.* (1987).

For samples (S2, S3, S4, S5 and S6) subjected to matric suction, they experienced a further decrease in void ratio when the net mean stress was increased to higher levels at constant matric suction condition.

In the last stress path where the matric suction was reduced to 25 kPa at constant applied net mean stress of 700 kPa, these samples again showed a decrease in the void ratio. The decrease in void ratio as a result of reduction of matric suction is normally termed as collapse. Similar collapsible behavior upon reduction of matric suction or upon wetting at constant net mean stress (or applied stress) was also reported by researchers such as El Sohby and Rabbaa (1984), El-Sohby and Elleboudy (1987), Lawton *et al.* (1989) and Tadepalli and Fredlund (1991).

It is of interest to note that at all levels of net mean stress, the void ratio of the samples (S2, S3, S4, S5 and S6) subjected to matric suction were significantly greater than that of the sample (S1) which was not subjected to matric suction throughout the test. For instance, sample S2 that was only subjected to a matric suction of 25 kPa, the void ratio of the sample was greater than that of sample S1 by approximately 0.10 at net mean stress

Bujang B. K. Huat, Faisal Hj. Ali and Choong Foong Heng

TABLE 3
Stress paths of samples tested

Sample S1

Stress Point	Net Mean Stress $(\sigma - u_a)$ (kPa)	Matric Suction $(u_a - u_w)$ (kPa)
A1	100	0
-	-	-
B1	200	0
C1	300	0
D1	400	0
E1	500	0
F1	600	0
G1	700	0
-	-	-

Sample S2

Stress Point	Net Mean Stress $(\sigma - u_a)$ (kPa)	Matric Suction $(u_a - u_w)$ (kPa)
A2	100	25
-	-	-
B2	200	25
C2	300	25
D2	400	25
E2	500	25
F2	600	25
G2	700	25
-	-	-

Sample S3

Stress Point	Net Mean Stress $(\sigma - u_a)$ (kPa)	Matric Suction $(u_a - u_w)$ (kPa)
A2	100	25
A3	100	50
B3	200	50
C3	300	50
D3	400	50
E3	500	50
F3	600	50
G3	700	50
G2	700	25

Sample S4

Stress Point	Net Mean Stress $(\sigma - u_a)$ (kPa)	Matric Suction $(u_a - u_w)$ (kPa)
A2	100	25
A4	100	100
B4	200	100
C4	300	100
D4	400	100
E4	500	100
F4	600	100
G4	700	100
G2	700	25

Sample S5

Stress Point	Net Mean Stress $(\sigma - u_a)$ (kPa)	Matric Suction $(u_a - u_w)$ (kPa)
A2	100	25
A5	100	200
B5	200	200
C5	300	200
D5	400	200
E5	500	200
F5	600	200
G5	700	200
G2	700	25

Sample S6

Stress Point	Net Mean Stress $(\sigma - u_a)$ (kPa)	Matric Suction $(u_a - u_w)$ (kPa)
A2	100	25
A6	100	250
B6	200	250
C6	300	250
D6	400	250
E6	500	250
F6	600	250
G6	700	250
G2	700	25

90

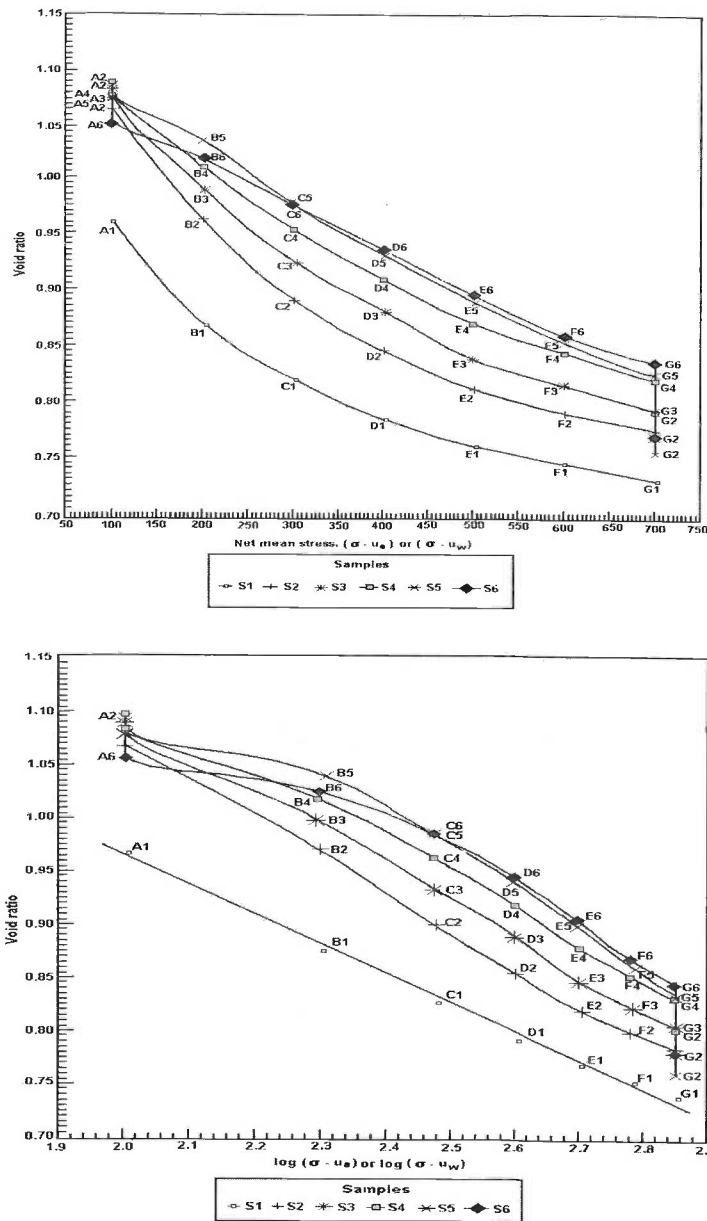Pertanika J. Sci. & Technol. Vol. 15 No. 2, 2007

Fig. 3: Void ratio of samples at various stress points

of 100 kPa and approximately 0.05 at net mean stress of 700 kPa. The void ratio of sample S6 which was subjected to a matric suction of 250 kPa was found to be greater than that of sample S1 by as significant as approximately 0.16 at net mean stress of 300 kPa. In addition, this difference in void ratio (between sample subjected to matric suction and sample not subjected to the matric suction) appeared to be relatively greater at lower net mean stress level and smaller at higher level of net mean stress.

The significant difference in void ratio showed that the matric suction applied on the sample appeared to have contributed to a pronounce effect on the volume change of the soil. It appears that the matric suction has provided an additional rigidity to the soil structure. This has in turn helped the soil to withstand greater net mean stress at a given void ratio or in other words, withstand a given net mean stress at a significantly greater void ratio. This could be the main reason why at a given net mean stress, the void ratio of samples subjected to the matric suction appeared to be significantly greater than that of sample not subjected to the applied matric suction.

The effect of the additional rigidity from the matric suction to the soil structure appeared to increase as the matric suction applied on the sample was increased. From *Fig. 3*, it can be noted that the void ratio of the sample subjected to higher matric suction was generally greater than that of sample subjected to lower matric suction. This is particularly apparent at the higher net mean stress levels.

However, when the applied matric suction was reduced to 25 kPa, the additional rigidity appears to decrease accordingly. The decrease in the additional rigidity would have then caused the instability of the soil structure and consequentially led to a collapses or reduction in void ratio without an increase in applied net mean stress.

Upon the reduction of the applied matric suction, it should be noted that samples S2, S3, S4, S5 and S6 were actually at the same stress point, G2 where the net mean stress and matric suction applied on the samples were similar. It is interesting to note that the void ratio of these samples appeared to be approximately close to each other at this stress point. This seems to suggest that there could be a uniqueness in the void ratio or at least an approximation to a uniqueness which represent a unique relationship between the void ratio of the soil and the stress variables i.e. matric suction and net mean stress. The similar uniqueness was also observed by Fredlund and Morgenstern (1976).

The collapsible behavior of the soil has a significant implication on the practical aspects of geotechnical design. When the unsaturated residual soil is used to construct engineering structure such as embankment, the soil is expected to experience suction if the structure is above the water table. The overburden pressure applied on the soil will gradually increase as the thickness of the soil increases during the construction stage. If the predicted settlement is derived from a conventional oedometer test (which is normally rewetted prior to the test), the actual settlement at the site caused by the increase in overburden pressure is therefore expected to be lower than the predicted value. However, after the completion of the project, the water table may rise due to the development at the adjacent area or due to other reasons, the matric suction of the soil would then decrease and thus collapse or serious settlement may occur. This would in turn cause serious damage to the structure constructed at such filled area.

CONCLUSIONS

From the results of this study, the following conclusions can be made with regard to the collapsibility and volume change behavior of unsaturated residual soil subjected to various levels of net mean stress and matric suction.

When the applied matric suction is first increased at constant net mean stress condition, the void ratio of the soil generally decreased. When the net mean stress is increased to higher levels at constant matric suction, the soil experience a further decrease in void ratio.

There is an apparent unique relationship between the void ratio, matric suction and net mean stress. The uniqueness in void ratio is observed when there is collapse (decrease in void ratio) due to the reduction in applied matric suction at constant net mean stress. This decrease (collapse) in void ratio is believed to be due to loss of additional rigidity provided by the suction to the soil structure as the suction is suddenly reduced.

At a similar net mean stress level, the void ratio of the soil subjected to matric suction of even as low as 25 kPa appear to have marked difference from soil not subjected to matric suction. Generally, when the soil is at the similar level of net mean stress, the void ratio of the soil subjected to applied matric suction is found to be significantly greater than that of sample not subjected to applied matric suction due to the additional rigidity provided by the matric suction to the soil structure.

REFERENCES

BOOTH, A.R. (1975). The factors influencing collapse settlement in compacted soils. *Proceedings of 4th International Conference on Expansive Soil* (p. 117-134). Colorado.

BISHOP, A.W. (1959). The principle of effective stress. *Teknish, Ukefland, 106*(39), 359-383.

CHIU, C.F. and NG, C.W.W. (2003). A state-dependent elasto-plastic model for saturated and unsaturated soils. *Geotechnique, 53*(9), 809-829.

EL-SOHBY, M.A. and RABBAA, A.A. (1984). Deformation behavior of unsaturated soil upon wetting. In *Proceedings of the 8th Regional Conference for African on Soil Mechanics and Foundation Engineering* (p. 129-137). Harare.

EL-SOHBY, M.A. and ELLEBOUDY, A.M. (1987). Swelling and collapsible behavior of cemented sand upon wetting. In *Proceedings of the 9th European Conference on Soil Mechanics and Foundation Engineering* (2, 553-556).

FREDLUND, D.G. and MORGENSTERN, N.R. (1976). Constitutive relation for volume change in unsaturated soils. *Canadian Geotechnical Journal, 13*(3), 261-276.

FREDLUND, D.G. and MORGENSTERN, N.R. (1977). Stress state variables for unsaturated soils. *ASCE Journal of Geotecnhical Engineering, 103*(5), 447-466.

FREDLUND, D.G. (1978). Appropriate concepts and technology for unsaturated soils. *Second Canadian Geoetchnical Colloqium,* 121-139.

FREDLUND, D.G., MORGENSTERN, N.R. and WIDGER, R.A. (1978). The shear strength of unsaturated soils. *Canadian Geotechnical Journal, 15*(3), 313-321.

FREDLUND, D.G. (1979). Second Canadian colloquium: Appropriate concepts and technology for saturated soils. *Canadian Geotechnical Journal, 16,* 121-139.

FREDLUND, D.G. and RAHARDJO, H. (1993). *Soil Mechanics for Unsaturated Soil.* New York: John Wiley & Sons.

HILF, J.W. (1956). *An investigation of pore water pressure in compacted cohesive soils.* Tech. Memorandum No. 654, Bureau of Reclamation. US Dept. of Interior.

JOSA, A., ALONSO, E.E., LLORET, A. and GEN, A. (1987). Stress-strain behavior of partially saturated soils. In *Proceedings of 9th European Conference on Soil Mechanics and Foundation Engineering* (2, 561-564).

LAWTON, E.C., FRAGASZY, R.J. and HARDCASTLE, J.H. (1989). Collapse of compacted clayey sand. *ASCE Journal of Geotechnical Engineering, 115*(9), 1252-1267.

LITTLE, A.L. (1969). The engineering classification of residual tropical soils. In *Proc. 7th International Conference Soil Mechanics and Foundation Engineering (1,* 1-10). Mexico.

McLEAN, A.C. and GRIBBLE, C.D. (1979). *Geology for Civil Engineers.* London: E & FN Spon.

NAGARAJ, T.S. and MURTHY, B.R.S. (1985). Compressibility of partially saturated soil. *ASCE Journal of Geotechnical Engineering, 111*(7), 937-942.

RAJ, J.K. (1985). Characterization of the weathering profile developed over a porphyritic granite in Peninsular Malaysia. In *Bulletin of the International Association of Engineering Geology (32,* 121-128). Paris.

SHARMA, R.S. and WHEELER, S.J. (2003). Behavior of an unsaturated highly expensive clay during cycles of wetting and drying. In *Proceedings Asian Conference on Unsaturated Soils* (p. 721-726). Singapore.

SINGH, H. and HUAT, B.B.K. (2004). Origin, formation and occurrence of tropical residual soils. In Huat *et al.* (Ed.), *Tropical residual soils engineering* (p. 1-20). Leiden, Balkema.

TADEPALLI, R. and FREDLUND, D.G. (1991). The collapse behavior of a compacted soil during inundation. *Canadian Geotechnical Journal, 28,* 447-488.

WHEELER, S.J., SHARMA, R.S. and BUISSON, M.S.R. (2003). Coupling of hydraulic hysteresis and strain-strain behaviour in unsaturated soils. *Geotechnique, 53*(1), 41-54.

Chemical Constituents from *Garcinia maingayi* and *Garcinia parvifolia* (Guttiferae) and Their Biological Activities

G.C.L. Ee and Y.L. Cheow
Department of Chemistry, Universiti Putra Malaysia,
43400 UPM, Serdang, Selangor, Malaysia
E-mail:gwen@fsas.upm.edu.my

ABSTRACT

Detail chemical studies on *Garcinia maingayi* have yielded one xanthone, 1,3,7-trihydroxy-2-(3-methylbut-2-enyl)-xanthone, one benzophenone, isoxanthochymol, one benzoic acid derivative 3,4-dihydroxy-methylbenzoate and two triterpenoids, stigmasterol and sitosterol. Meanwhile, investigations on *Garcinia parvifolia* have afforded one triterpenoid, α-amyrin and two xanthones, cowanin and rubraxanthone. Their structures were derived based on spectroscopic evidence, mainly 1D and 2D NMR spectroscopy. Acetylation reaction was carried out on rubraxanthone to yield triacetate rubraxanthone. It was found that the pure rubraxanthone was strongly active against the larvae of *Aedes aegypti* with LC_{50} value of 15.49 μg/ml and HL-60 cells line with an IC_{50} value of 7.5 μg/ml.

Keywords: *Garcinia maingayi, Garcinia parvifolia*, **1,3,7-trihydroxy-2-(3-methylbut-2-enyl)-xanthone, isoxanthochymol, 3,4-dihydroxy-methylbenzoate, cowanin, rubraxanthone, triacetate rubraxanthone**

INTRODUCTION

Garcinia is best known in Malaysia as a genus of fruit trees. The genus has been the subject of phytochemical studies which revealed it to be a major source of prenylated xanthones, benzophenones and biflavanoids linked between C-3 and C-8 (Xu *et al.*, 2001; Hussain and Waterman, 1982). Some of these exhibit a wide range of biological and pharmacological activities namely cytotoxic, anti-inflammatory, antimicrobial and antifungal activity (Minami *et al.*, 1996; Minami *et al.*, 1994). A number of *Garcinia* species have been investigated but only a few have been extensively studied. *Garcinia mangostana* and *Garcinia subelliptica* are the two species that have been well studied (Minami *et al.*, 1996; Minami *et al.*, 1994; Bennett and Lee, 1989; Iinuma *et al.*, 1995; Iinuma *et al.*, 1994; Asai *et al.*, 1995; Fukuyama *et al.*, 1991; Nilar and Harrison, 2002). There is no previous record on the chemistry and bioactivity of *Garcinia maingayi*.

MATERIAL AND METHODS

Plant Material

The stem bark of *Garcinia maingayi* and *Garcinia parvifolia* were collected from Fraser's Hill in Pahang. Voucher specimens are kept in the Institute of Bioscience, University Putra Malaysia.

General

Infrared spectra were measured in a KBr/NaCl pellet on a Perkin-Elmer FTIR Spectrum BX spectrometer. EIMS were recorded on a Shimadzu GCMS-QP5050A spectrometer. NMR spectra were obtained using a Unity INOVA 500 MHz NMR/ JEOL 400 MHz FT NMR spectrometer with tetrametylsilane (TMS) as internal standard. Ultra violet spectra were recorded on a Shimadzu UV-160A, UV-Visible Recording Spectrometer. Chromatographic separation was carried out using silica gel Merck 9385 and Sephadex LH-20.

Extraction and Isolation of Compounds

The dried and powdered stem bark material (1.5 kg each) of *Garcinia maingayi* and *Garcinia parvifolia* were extracted successively with distilled *n*-hexane, chloroform, acetone and methanol twice for 48 hours. About 12.8 g of crude hexane extract was fractionated by column chromatography over silica gel to yield stigmasterol (**1**) and sitosterol (**2**). The other three extracts were also subjected to a silica gel column chromatography and Sephadex LH-20 column to give isoxanthochymol (**3**), 1,3,7-trihydroxy-2-(3-methylbut-2-enyl)-xanthone (**4**) and 3,4-dihydroxymethylbenzoate (**5**). Fractionation of the hexane extract of *Garcinia parvifolia* (6.5 g) over a silica gel column yielded α-amyrin (**6**). Similarly, the chloroform extract was directly chromatographed on a silica gel column to give 20 fractions which when further purified in a Sephadex LH-20 column, gave cowanin (**7**). Rubraxanthone (**8**) was recrystallized as pale yellow powder in acetone after it was obtained from the column chromatography of the acetone extract.

Synthesis of Triacetate Rubraxanthone (9)

Acetylation of (**8**) was carried out by dissolving (**8**) (30 mg) in pyridine (3 ml) and acetic anhydride (3 ml). The solution was left at room temperature for 24 hours. The reaction mixture was poured into iced distilled water and then extracted with ethyl acetate. The organic extract was evaporated to dryness and purified by silica gel column chromatography to yield triacetate rubraxanthone (**9**).

Isoxanthochymol (**3**): White prisms, mp 125-127 °C. UV (EtOH) λ_{max} nm (log ε): 278 (1.24), 233 (1.10). IR ν_{max} cm^{-1} (KBr): 3648, 2974, 2938, 1718, 1680, 1640, 1606, 1454, 1366, 1184. CI-MS m/z (rel. int.): 603 (M+1) (5), 469 (10), 391 (10), 279 (15), 221 (15), 149 (100), 113 (22), 74 (42). ^{1}H NMR and ^{13}C NMR see Table 1.

1,3,7-trihydroxy-2-(3-methylbut-2-enyl)-xanthone (**4**): Pale yellow needles, mp 211-213°C (Harrison *et al.*, 1993, 217-218°C). UV (EtOH) λ_{max} nm (log ε): 239.5 (1.36), 262.5 (1.28), 313.5 (0.66), 377.0 (0.25). IR ν_{max} cm^{-1} (KBr):3438 2924, 1786, 1642. EI-MS m/z (rel. int.): 312 [M$^+$, 48], 297 (37), 269 (82), 257 (100), 244 (16), 229 (11), 137 (12), 115 (10), 77 (12), 65 (19), 53 (19), 41 (20). ^{1}H NMR and ^{13}C NMR data agree with literature values (Harrison *et al.*, 1993).

Cowanin (**7**): Yellowish oil. ^{1}H NMR and ^{13}C NMR data are in agreement with published data (Harrison *et al.*, 1993).
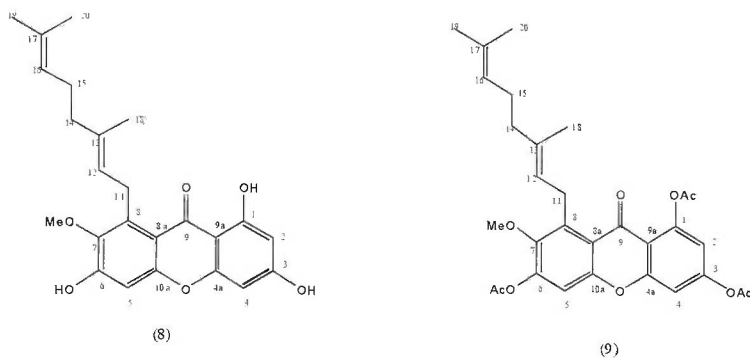
(1)

(2)

(3)

(4)

(5)

(6)

(7)

(8)

(9)
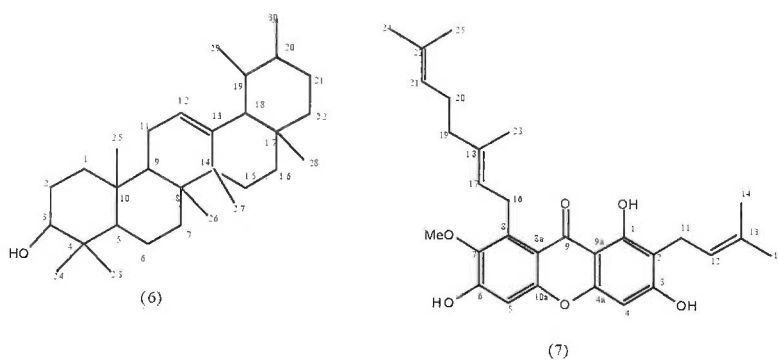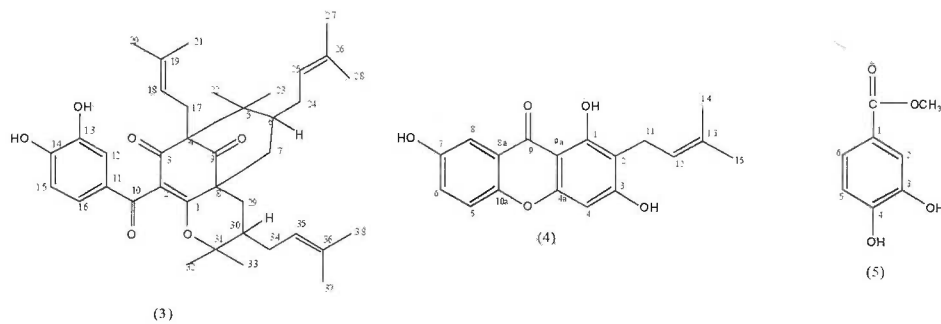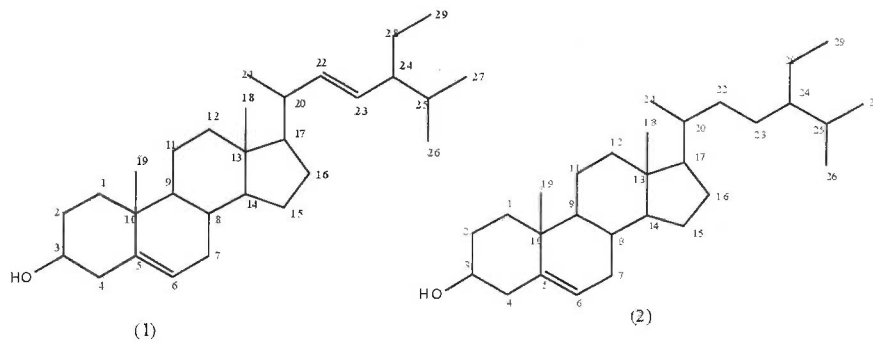
TABLE 1
NMR data for isoxanthochymol (3)

Position	^{1}H (δ)	^{13}C (δ)	Position	^{1}H (δ)	^{13}C (δ)
6	1.44 (1H, m)	45.3	22	1.04 (3H, s)	22.3
7	2.14 (Ha, bd, J = 14.3Hz)	38.3	23	0.90 (3H, s)	26.4
	2.01 (H$_b$, dd, J =6.8,14.3Hz)				
8	-	50.9	24	2.87 (Ha, m)	27.8
				1.02 (H$_b$, m)	
9	-	206.9	25	4.92 (1H, m)	125.3
10	-	193.7	26	-	132.4
11	-	129.0	27	1.65 (3H, s)	25.9
12	7.13 (1H, s)	115.4	28	1.50 (3H, s)	18.0
13	-	145.4	29	1.80 (2H, m)	29.2
14	-	151.2	30	1.36 (1H, m)	42.5
15	6.74 (1H, d, J = 8.3 Hz)	115.2	31	-	86.7
16	6.94 (1H, d, J = 8.3 Hz)	122.2	32	0.83 (3H, s)	28.5
17	2.48 (Ha, d, J = 13.7 Hz)	26.0	33	1.18 (3H, s)	21.2
	2.34 (H$_b$, m)				
18	4.78 (1H, m)	120.7	34	1.99 (Ha, m)	29.0
				2.58 (H$_b$, m)	
19	-	132.9	35	5.18 (1H, m)	122.2
20	1.51 (3H, s)	26.0	36	-	133.1
21	1.60 (3H, s)	18.2	37	1.73 (3H, s)	26.0
			38	1.59 (3H, s)	18.2

Rubraxanthone (8): Pale yellow powder, mp 208-210 °C (Ampofo and Waterman, 1986, 205-206 °C). UV (EtOH) λ_{max} nm (log ϵ): 432 (0.12), 312 (1.06), 240 (1.60), 214 (1.06). IR ν_{max} cm^{-1} (KBr): 3446, 2970, 1648, 1606,1466. EI-MS m/z (rel. int.): 410 (30), 341 (100), 326 (11), 311 (42), 299 (55), 288 (20), 271 (12), 69 (50), 41 (62). ^{1}H NMR (400 MHz, Me$_2$CO): δ 13.42 (1H, s, OH-1), 6.76 (1H, s, H-5), 6.23 (1H, s, H-4), 6.11 (1H, d, J = 1.8 Hz, H-2), 5.19 (1H, t, J = 6.4Hz, H-12), 4.95 (1H, t, J = 7.4 Hz, H-16), 4.04 (2H, d, J = 6.4 Hz, H-11), 3.71 (3H, s, 7-OCH$_3$), 2.09 (2H, t, J = 7.4 Hz, H-15), 1.90 (2H, t, J = 7.4 Hz, H-14), 1.83 (3H, s, H-18), 1.47 (3H, s, H-19), 1.43 (3H, s, H-20). ^{13}C NMR (100 MHz, Me$_2$CO): δ 181.9 (C-9), 164.6 (C-1), 164.1 (C-3), 157.2 (C-4a), 156.8 (C-6), 155.5 (C-10a), 143.8 (C-7), 137.4 (C-8), 134.3 (C-13), 130.8 (C-17), 124.4 (C-12), 124.3 (C-16), 111.2 (C-8a), 102.9 (C-5), 102.2 (C-9a), 97.9 (C-2), 93.0 (C-4), 60.3 (OCH$_3$), 39.6 (C-14), 26.5 (C-11), 25.5 (C-15), 25.0 (C-19), 16.9 (C-20), 15.8 (C-18).

Triacetate rubraxanthone (9): White crystal, mp 122-124°C. UV (EtOH) λ_{max} nm (log ϵ): 341 (0.16), 271 (2.04), 203 (0.76)IR ν_{max} cm^{-1} (KBr): 2968, 1658, 1604. ^{1}H NMR (400 MHz, Me$_2$CO): δ 8.50 (1H, s, H-5), 7.82 (1H, d, J = 2 Hz, H-2, H-4), 5.90 (1H, t, J = 6.0 Hz, H-12), 4.85 (1H, t, J = 6.0Hz, H-16), 4.69 (2H, d, J = 6.0 Hz, H-11), 3.98 (3H, s, OMe), 2.80 (3H, s, OAc), 2.85 (6H, s OAc), 1.37 (3H, s, H-18), 1.36 (3H, s, H-19, H-20), ^{13}C NMR (100 MHz, Me$_2$CO): δ 201.0 (3 x C=O), 176.0 (C-9), 168.9 (C-1), 168.4 (C-3), 168.2 (C-6), 157.1 (C-4a), 155.3 (C-10a), 147.7 (C-7), 138.7 (C-8), 135.3 (C-13), 131.1 (C-17), 124.7 (C-16), 123.5 (C-12), 118.8 (C-8a), 113.7 (C-9a), 113.4 (C-5), 111.2 (C-2), 108.7 (C-4), 61.5 (OMe), 40.0 (C-14), 26.8 (C-15), 26.0 (C-11), 25.3 (C-19), 20.7 (OAc), 20.6(OAc), 20.3 (OAc), 17.2 (C-20), 16.2 (C-18).

TABLE 2

Cytotoxic activity of plant extracts and pure compound against HL-60 Cell Line (Promyelocytic Leukemia) and CEM- SS Cell Line (T lymphoblastic Leukemia)

Plant	Extracts/Pure Compounds	IC_{50} (μg/ml)
Garcinia maingayi	Hexane	10.0
[Against HL-60 cell line (Promyelocytic Leukemia)]	Chloroform	26.5
Garcinia parvifolia	Hexane	16.5
[Against CEM-SS cell line (T-lymphoblastic Leukemia)	Chloroform	6.5
	Acetone	19.5
	Rubraxanthone (8)	7.5
	Triacetate rubraxanthone (9)	10.3

TABLE 3

Larvicidal activity of crude extracts and pure compound against the larvae of *Aedes aegypti*

Plants	Extracts / *Pure compound	LC_{50} (μg/ml)	LC_{90} (μg/ml)
Garcinia maingayi	Hexane	145.95	249.60
	Chloroform	N.A	N.A
	Acetone	250.58	281.74
	Methanol	209.52	292.45
Garcinia parvifolia	Hexane	98.54	225.91
	Chloroform	92.07	223.80
	Acetone	67.98	192.12
	Rubraxanthone* (8)	15.49	21.30
	Triacetate rubraxanthone* (9)	N.A	N.A

N.A = Not Active

Bioassay

Bioassay on the crude extracts and pure compounds were performed on the larvae of *Aeds aegypti* according to the protocols of the World Health Organisation (1981). Cytotoxic assays were carried using the HL-60 and CEM-SS cells line. The cells were cultured and maintained in growth medium as described by Ali *et al.* (1996).

RESULTS AND DISCUSSION

Compound (3) was obtained as white prisms, with m.p 125-127 °C. The $(M+1)^+$ at m/z 603 in the CI-MS corresponds to the molecular formula $C_{38}H_{50}O_6$. UV absorptions at 277 and 233 nm revealed a chromophore with extended conjugation. The FTIR spectrum showed strong bands for a hydroxyl group at 3468 cm^{-1} and both non-conjugated and conjugated carbonyl groups at 1718 and 1680 cm^{-1}.

Three vinylic protons, six vinylic methyl protons and six allylic protons were apparent in the ^{1}H NMR spectrum of (3) indicating the presence of three isoprenyl groups. The characteristic 3,4-dihydroxy benzoyl group was evident from proton resonance at δ 7.13 (1H, s), δ 6.94 (1H, d, J = 8.3 Hz) and δ 6.74 (1H, d, J = 8.3 Hz) which were assigned to H-12, H-16 and H-15 respectively. The large coupling constant indicated that H-15 and

H-16 are *ortho*-coupled aromatic protons. In addition to that, the methylene and methine protons which gave complexes of multiplets of 12H in the regions of δ 1.3 to 2.9 were observed. The ^{1}H NMR also showed 4 tertiary methyl protons which accounted for H-22, H-23, H-32 and H-33. Additional evidence for three ketone functions inferred from the FTIR spectrum was obtained from the ^{13}C NMR spectrum.

Characteristic ^{13}C NMR resonances for substituted aromatic carbons at δ 129.0 (C-11), δ 145.4 (C-13) and δ 151.2 (C-14) and a conjugated carbonyl group [δ 193.7, (C-10)] confirmed the existence of a 3,4-dihydroxy benzoyl group. Resonances consisting of a non-conjugated ketone at δ 206.9 (C-9) flanked by two quaternary carbons at δ 67.7 (C-4) and δ 50.9 (C-8) were also observed. HMBC established the substitution pattern of the isoprenyl group in (**3**). The methylene protons of H-17 gave a cross peak to C-9 thus suggesting one of the prenyl group is located at C-4. No correlation for the other two prenyl groups was observed to identify their substitution patterns. However based on previous reports on (**3**), (Gustasfson *et al.*, 1992) the two other prenyl moieties were placed at C-6 and C-30. The presence of isoprenyl moieties was further validated by HMBC. The methyl protons of H-37 [δ 1.73 (3H, s)], H-38 [δ 1.59 (3H, s)], H-27 [δ 1.65 (3H, s)], H-28 [δ 1.50 (3H, s)], H-20 [δ 1.51 (3H, s)] and H-21 [δ 1.60 (3H, s)] all showed linkages to the carbon atoms C-35 (δ 122.2), C-36 (δ 133.1), C-25 (δ 125.3), C-26 (δ 132.4), C-18 (δ 120.7) and C-19 (δ 132.9). Compound (**3**) was therefore identified as isoxanthochymol and the spectral data are summarized in Table 1.

Compound (**8**) was obtained as a yellow powder, mp.: 208-210 °C (Ampofo and Waterman, 1986, 205-206 °C). The [M$^+$] at m/z 410 in the EI-MS spectrum corresponds to the molecular formula $C_{24}H_{26}O_6$. The ^{1}H NMR spectra revealed signals for a H-bonded hydroxyl function (δ 13.4) at C-1 and three aromatic protons two of which are *meta*-coupled [δ 6.23 (1H, s), δ 6.11 (1H, d, *J* = 1.8Hz)] for H-4 and H-2] and a singlet at δ 6.76 for H-5. A single methoxy resonance occurred at δ 3.71. The remaining resonances appeared as a series of signals typical of a geranyl moiety. Also observed were an olefinic methyl proton at δ 1.83 (3H, s, H-18), a geminal-dimethyl protons at δ 1.47 (3H, s, H-19) and δ 1.43 (3H, s, H-20) in addition to a methylene proton at δ 4.04 (2H, d, *J* = 6.4Hz, H-11) and two vinyl methine protons at δ 5.19 (1H, t, *J* = 6.4Hz, H-12) and δ 4.95 (1H, t, *J* = 7.4Hz, H-16). Other than that, the ^{1}H NMR spectrum also exhibited two sets of methylene protons at δ 1.90 (2H, t, *J* = 7.4Hz) and δ 2.09 (2H, m) attributable to H-14 and H-15. The signal of the methylene proton (δ 4.04) of the chain which appeared in the low field region indicated that the geranyl group was located at C-8 which is next to the carbonyl group.

The ^{13}C NMR spectrum clearly showed 24 carbon signals. A typical conjugated carbonyl group (δ 181.9, C-9) for xanthones was observed. From the ^{13}C NMR spectrum six aromatic carbons with O-function appeared at δ 164.6, δ 164.1, δ 157.2, δ 156.8, δ 143.8 and δ 137.4. These were assigned to C-1, C-3, C-4a, C-6, C-7 and C10a respectively. The resonance at δ 60.3 was due to a methoxy group. These suggests that (**8**) is a tetraoxygenated xanthone with one methoxy and three hydroxyl group. From the DEPT spectrum five methine, three methylene, three methyl and twelve tertiary carbon signals were observed supporting the structure for rubraxanthone (**8**), previously isolated from *Garcinia pyrifera* (Ampofo and Waterman, 1986).

Rubraxanthone triacetate (**9**) was obtained from the acetylation reaction on rubraxanthone (**8**). Recrystalization from acetone gave the triacetate as an amorphous white solid, of m.p 122-124 °C. The [M$^+$] at m/z 536 in the EI-MS spectrum corresponds to the molecular formula $C_{30}H_{32}O_9$. The IR spectrum didn't display any hydroxyl

functional groups indicating they were successfully replaced by the acetyl moieties. From the ^{1}H NMR spectrum, the absence of the chelated hydroxyl group further supports that the acetylation chemical reaction has replaced the hydroxyl groups in (**8**). As compared to (**8**), chemical shifts for the aromatic, vinylic and methylene protons in triacetate rubraxanthone (**9**) have appeared more down field at δ 8.50 (1H, s, H-5), δ 7.82 (1H, d, J = 2 Hz, H-2, 1H, d, J = 2 Hz, H-4), δ 5.90 (1H, t, J = 6.0 Hz, H-12) and δ 4.69 (2H, d, J = 6.0 Hz, H-11) due to anisotropic effect. The presence of the methyl protons of the acetate group was confirmed by the ^{1}H NMR spectrum at δ 2.80 (3H, s, OAc). The two other methyl protons were observed at δ 2.85.

The ^{13}C NMR spectrum exhibited the typical conjugated carbonyl group at δ 176.0 (C-9) together with six oxygenated aromatic carbons at δ 168.9 (C-1), δ 168.4 (C-3), δ 168.2 (C-6), δ 157.1 (C-4a), δ 155.3 (C-10a) and δ 147.7 (C-7). The methine aromatic carbons resonances appeared at δ 113.4 (C-5), δ 111.2 (C-2) and 108.6 (C-4) in the lower field region due to anisotropic effect by the ketone group of acetyl moieties. The methyl carbons for the acetyl groups were observed at δ 20.7 (OAc), δ 20.6 (OAc), δ 20.3 (OAc).

The other compounds, stigmasterol (**1**), sitosterol, (**2**), 1,3,7-trihydroxy-2-(3-methylbut-2-enyl)-xanthone (**4**), 3,4-dihydroxy-methylbenzoate (**5**), α-amyrin (**6**) and cowanin (**7**) were identified by spectral data and by comparison with literature data (Harrison *et al.*, 1993; Holland *et al.*, 1978).

All the crude extracts and pure compounds obtained were bioassayed against the larvae of *Aedes aegypti*. It was found that the crude hexane, acetone and methanol extract of *Garcinia maingayi* were weakly active against the larvae with LC_{50} values of 145.9, 250.58 and 209.58 mg/ml respectively. The hexane, chloroform and acetone extract of *Garcinia parvifolia* showed moderate activities against the larvae by giving LC_{50} values of less than 100 μg/ml. Pure rubraxanthone (**8**) exhibited a strong activity against the larvae with LC_{50} value of 15.49 μg/ml. However, its derivative triacetate rubraxanthone (**9**) did not display any toxicity against the larvae. This suggests that the hydroxyl functional groups could be responsible for the toxicity against the larvae.

Biological activities of crude extracts and pure compounds were also carried out against HL-60 and CEM-SS cancer cells line. The crude hexane and chloroform extracts of *Garcinia maingayi* were considered to be active against HL-60 cell line with the IC_{50} values of less than 30 μg/ml. Meanwhile, the crude hexane and acetone extracts of *Garcinia parvifolia* were also considered to be active against CEM-SS cells line with the IC_{50} values of less than 30 μg/ml; meanwhile the crude chloroform extract showed a significant activity with an IC_{50} value of 6.5 μg/ml. Pure rubraxanthone (**8**) exhibited a strong activity against CEM-SS cell line with the IC_{50} values of 7.5 μg/ml. However the replacement of the hydroxyl groups on (**9**) didn't cause any significant change to its toxicity against the cancer cell lines

ACKNOWLEDGEMENT

REFERENCES

ALI, A.M., MACKEEN, M.M., SAFINAR, I.I., HAMID, M., LAJIS, N.H., EL-SHARKAWY, S.H and MURAKOSHI,M. (1996). Antitumor promoting and antitumor activities of the crude extract from the leaves of *Juniperus chinensis. Journal of Ethnopharmacology, 53,* 165-169.

AMPOFO, S.A, and WATERMAN, P.G. (1986). Xanthones from *Garcinia* species. *Phytochemistry, 25*(10), 2351-2355.

ASAI, F., TOSA, H., TANAKA, T. and IINUMA, M. (1995). A xanthone from pericarps of *Garcinia mangostana. Phytochemistry, 39*(4), 943-944.

BENNETT, G.J. and LEE, H.H. (1989). Xanthones from Guttiferae. *Phytochemistry, 28*(4), 968-998.

CHLOP, A. (1965). *Dictionary of Organic Compounds.* (p. 228).

FUKUYAMA, Y., KAMIYAMA, A., MIMA, Y. and KODAMA, M. (1991). Prenylated xanthones from *Garcinia sublliptica. Phytochemistry, 30*(10), 3433-3436.

GUSTASFSON, K.R., BLUNT, J.W., MUNRO, M.H.G., FULLER, R.W., MCKEE, T.C., CARDELLINA, J.H., MCMAHON, J.B., CRAGG, G.M. and BOYD, M.R. (1992). The guttiferones, HIV-inhibitory benzophenones from *Symphonia globulifera, Garcinia livingstonei, Garcinia ovalifolia* and *Clusia rosea. Tetrahedron, 48*(46), 10093-10102.

HARRISON, L.J, LEONG L. S., SIA G.L., SIM K.Y. and TAN H.T.W. (1993). Xanthones from *Garcinia forbesii. Phytochemistry, 33*(3), 727-728.

HOLLAND, H.K., DIAKOW, P.R.P. and TAYLOR, G.J. (1978). ^{13}C Nuclear magnetic resonance spectra of some C-19 hydroxy, C-5, 6 epoxy and C-24 ethyl steroids. *Canada Journal of Chemistry, 56,* 3121-3127.

HUSSAIN, R.A. and WATERMAN P.G. (1982). Lactones, flavonoids and benzophenones form *Garcinia conrauna* and *Garcinia manii. Phytochemistry, 21*(6), 1393-1396.

IINUMA, M., TOSA, H., TANAKA, T., SHIMANO, R., ASAI, F. and YONEMORI, S. (1994). Two xanthones from root bark of *Garcinia subelliptica. Phytochemistry, 35*(5), 1355-1360.

IINUMA, M., TOSA, H., TANAKA, T., SHIMANO, R. and ASAI, F. (1995). Three xanthones from root bark of *Garcinia subelliptica. Phytochemistry, 38*(1), 247-249.

MINAMI, H., KINOSHITA, M., FUKUYAMA, Y., KODAMA, M., YOSHIZAWA, T., SUGIURA, M., NAKAGAWA, K. and TAGO, H. (1994). Antioxidants xanthones from *Garcinia subelliptica. Phytochemistry, 36*(2), 501-506.

MINAMI, H., TAKAHASHI, E., KODAMA, M. and FUKUYAMA, Y. (1996). Three xanthones from *Garcinia subelliptica. Phytochemistry, 41*(2), 629-633.

NILAR and HARRISON, L. J. (2002). Xanthones from the heartwood of *Garcinia mangostana. Phytochemistry, 60,* 541-548.

WORLD HEALTH ORGANIZATION. *Instruction for determining the susceptibility or resistance of mosquito larvae to insecticides* (WHO/VBC/81.807).

XU, Y.J., LAI, Y.H., IMIYABIR, Z. and GOH, S.H. (2001). Xanthones from *Garcinia parvifolia. Journal of Natural Product, 64,* 1191-1195.

Skin Colour Detection Based on an Adaptive Multi-Thresholding Technique

**Ahmed M. Mharib[1], Mohammad Hamiruce Marhaban[2]
and Abdul Rahman Ramli[1]**

*Departments of [1]Computer and Communication Systems Engineering
and [2]Electrical and Electronic Engineering
Faculty of Engineering, Universiti Putra Malaysia
E-mail: ahmad_muhdrrn@yahoo.com*

ABSTRACT

Skin colour is an important visual cue for face detection, face recognition, hand segmentation for gesture analysis and filtering of objectionable images. In this paper, the adaptive skin color detection model is proposed, based on two bivariate normal distribution models of the skin chromatic subspace, and on image segmentation using an automatic and adaptive multi-thresholding technique. Experimental results on images presenting a wide range of variations in lighting condition and background demonstrate the efficiency of the proposed skin-segmentation algorithm.

Keywords: Skin colour detection, adaptive multi-thresholding technique, skin-segmentation algorithm

INTRODUCTION

The skin colour detection algorithm is used as a post-processing step in order to separate skin regions from the background of a scene and treats the skin regions as candidate faces or hands for detecting and tracking. In pixel-based skin detection methods, the task can be considered as a standard two-class classification problem. This method will take each pixel of the input image and produce abinary output image ('1' represents skin pixel and '0' represents non-skin pixel). Pixel-based skin detection methods can be classified into three categories as shown in *Fig. 1* (Terrillon *et al.*, 2000; Vezhnevets and Andreeva, 2005; Vezhnevets *et al.*, 2003; Gomez and Morales, 2002; Lee and Yoo, 2002; Zarit *et al.*, 1999; Hsu *et al.*, 2002; Zhu *et al.*, 2004).

The parametric statistical approaches represent the skin-colour distribution in the parametric form, such as the Gaussian mode. A Gaussian distribution is a symmetrical frequency distribution having a precise mathematical formula relating the mean and standard deviation of the samples. The probability distribution function (PDF) used to describe the probability of the variant to belong to the group of data which have Gaussian distribution. A more sophisticated model, capable of describing complex-shaped distributions is the Mixture of Gaussians model (GMM) (Mukhopadhyay, 2000).

This work consists of two main steps. First, skin detection model Single Gaussia model (SGM) and GMM of the skin-color distribution are built based on sample pixels taken from a large number of people and in different lighting conditions. Second, skin-colour segmentation is performed based on the SGM and GMM of the skin-colour distribution, where an automatic adaptive thresholding technique is used to segment an image into skin and non-skin regions.
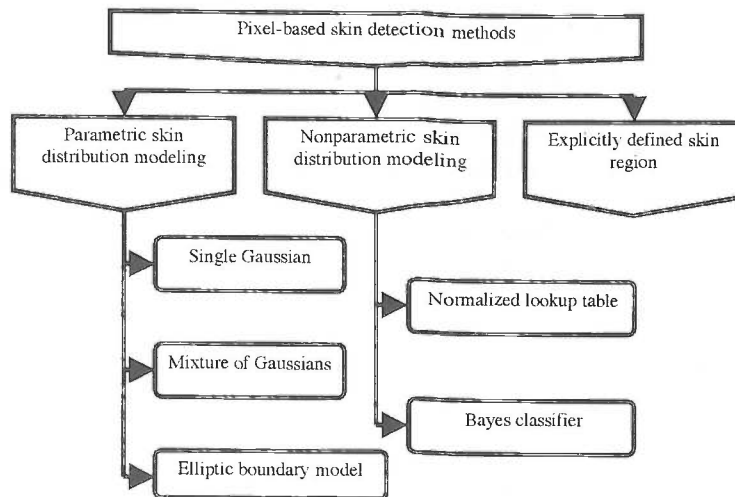
Ahmed M. Mharib, Mohammad Hamiruce Marhaban and Abdul Rahman Ramli

Fig. 1: Pixel-based skin detection methods

TRAINING DATA COLLECTION AND COLOR SPACE TRANSFORMATION

To cover a wide range of skin chromatic characteristics, 1000 skin samples (64×64 pixels) were used. These samples were extracted by using the Photoshop program from the JPEG image files collected from random sites, and from the different face database (7 face database). TSL (T is a tint value, S is a saturation value, L is a luminance value) colour space was chosen in this research. L component is eliminated to reduce the complexity of modeling the skin distribution into 2D model (Caetano and Barone, 2001). *Fig. 2* shows the 3D histogram distribution of the training data in TSL color space.
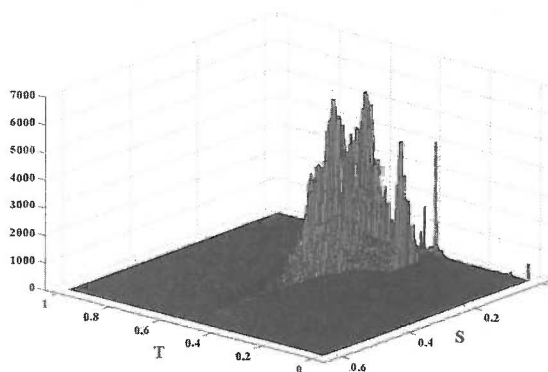
Fig. 2: 3D histogram distribution of training data in TSL color space

From *Fig. 2,* it is obvious that the skin data distribution is clustered into two groups referred to as C1 and C2, which make the decision of considering the GMM with two components more reasonable.

SGM AND GMM PARAMETERS ESTIMATION

The SGM parameters estimation was done by applying a simple mathematical operation on the collected training data as follows (Mukhopadhyay, 2000):

$$\mu_s = \frac{1}{N-1} \sum_{j=0}^{s-1} \mathbf{x}_j \tag{1}$$

$$\Sigma_s = \frac{1}{N-1} \sum_{j=1}^{N} (\mathbf{x}_j - \mu_s)(\mathbf{x}_j - \mu_s)^T \tag{2}$$

Where μ_s is the mean vector and Σ_s is the covariance matrix, N is the total number of pixels and X is the color component of the training data.

GMM parameters estimation is more complicated than SGM. In this paper, the Expectation-Maximization algorithm is used for this purpose (Phung *et al.*, 2005). Two Gaussian components are used to represent the distribution of the skin colour in the GMM. The EM algorithm is run on the training data until the difference between the consecutive likehood-function values is an accepted small value.

THE SKIN DETECTION MODEL

The proposed skin detection model (SDM) is constructed based on the SGM and the GMM. Each one of them detects the skin pixels of a still image separately, then an OR logical operation is applied on the skin map images. Thus any pixel that will be detected as skin by any one of these two models will be considered as skin pixel. The estimated parameters values of SGM and the two Gaussian components of the GMM (C1 and C2) are substituted in the PDF. The following expressions introduce the used skin detector model in this paper (Gokalp, 2005).

$$P(T,S|\Theta) = \frac{a}{2\pi\sigma_T\sigma_S\sqrt{1-\rho^2}} \times e^{\frac{-1}{2(1-\rho^2)} \times \left[\frac{(T-\mu_T)^2}{\sigma_T^2} - \frac{2\rho(T-\mu_T)(S-\mu_S)}{\sigma_T \times \sigma_S} + \frac{(S-\mu_S)^2}{\sigma_S^2} \right]} \tag{3}$$

$$\rho = \frac{\sigma_{TS}}{\sigma_T . \sigma_S} \tag{4}$$

$$P(T,S|\Theta)_{GMM} = P(T,S|\Theta)_{C1} + P(T,S|\Theta)_{C2} \tag{5}$$

Where T and S represent the Tint value and Saturation value in TSL color space of the tested pixel respectively, (μ_T, σ_T) and (μ_s, σ_s) represent the training data mean and standard deviation of Tint and Saturation respectively, σ_{TS} represent the training data covariance of Tint and Saturation and represent the probability of each pixel to be classified as a skin. The probability maps of SGM and the GMM are shown in *Fig. 3*.
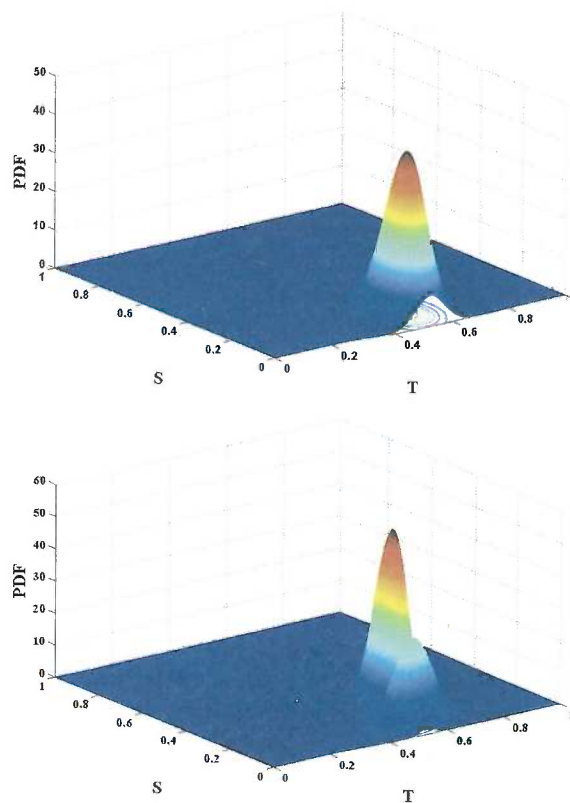
Fig. 3: The probability map of skin color distribution (a: SGM and b: GMM)

THE OPTIMAL THRESHOLD VALUE ESTIMATION

An automatic and adaptive multi-thresholding estimation technique is used to obtain the optimal threshold values of the SGM and the GMM. The following procedures illustrate how these values are estimated:

1. Each pixel in the input test image will be applied in the PDF of the SGM and GMM.
2. Pixels with the probability less than 0.1 will be neglected.
3. The average of the pixel's probabilities (greater than 0.1) will be calculated for the SGM and the GMM (APSG and APGM).
4. $(thr)_{SGM} = F_{GM} \times APSG$ and $(thr)_{SGM} = APSG$. Where F_{SGM} is the threshold factor of SGM, and F_{GMM} is the threshold factor of GMM.

F_{SGM} and F_{GMM} will be estimated graphically. *Figs. 4* and *5* show different behaviours for almost all the relationships between the threshold factor values and the error rate of SGM and GMM respectively, for test example images. The evaluation of the error rate is considered both for the non-skin pixels classified as skin and real skin pixels classified as the non-skin. The following expression explains this:

$$ER = (\frac{SCN}{number\ of\ real\ skin\ pixels} + \frac{NCS}{number\ of\ non\ skin\ pixels}) \times 100 \qquad (6)$$

Where SCN is the number of the real skin pixels in the test image which has been classified as non-skin; and NCS is the number of the non-skin pixels which have been classified as skin.
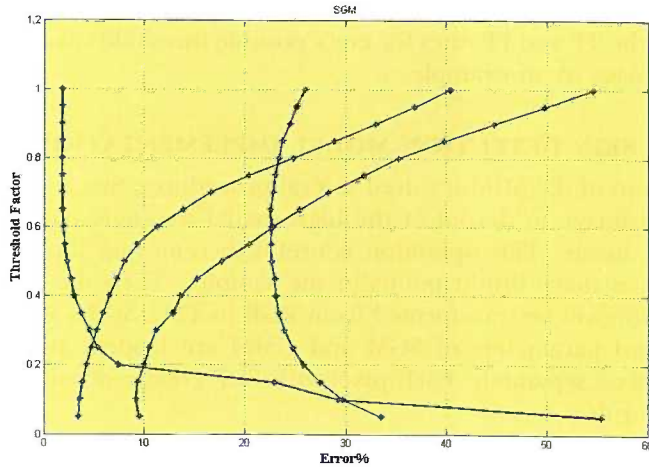
Fig. 4: Examples of the relationship between the threshold factor values and the error rate in SGM
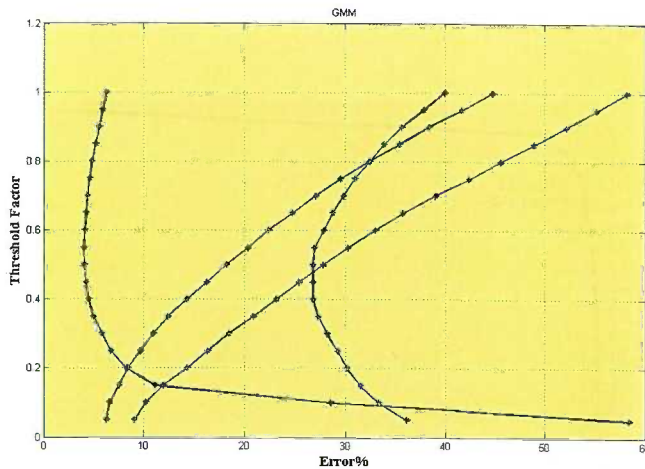

Fig. 5: Examples of the relationship between the threshold factor values and the error rate in GMM

The threshold value factors should be chosen in the range where the error is minimum. Unfortunately, some test images have the minimum error rate when the threshold factor is a small value, and others have it when the threshold factor is a bigger value. In this case, appropriate values should be used for all possible conditions. From *Figs. 4* and *5*, it can be observed that the threshold values of the SGM and GMM in the range from 0.2 to 0.4 represent a suitable choice.

THRESHOLD VALUE FACTOR

The threshold value factor plays an important part in the skin detection process. The results show that by decreasing F_{SGM} and F_{GMM}, The True Positive (TP) and The False Positive (FP) increased, and by increasing F_{SGM} and F_{GMM}, TP and FP decreased. In this paper, Receiver Operating Characteristic (ROC) is used as graphical representation of the trade off between the TP and FP rates for every possible threshold value factor. *Fig. 6* shows a ROC of a test image as an example.

SKIN DETECTION MODEL IMPLEMENTATION

The implementation of the SDM involved several procedures, first a spatial low pass filter is used with input image to devoid of the high spatial frequency components that may be present in the image. This operation is useful in removing the visual noise, which generally appears as sharp bright points in the samples. Then the input image colour space representation will be transformed from RGB to TSL. At the stage of applying the SDM, the estimated parameters of SGM and GMM are loaded, and the SDM will be applied on each pixel separately. Each pixel with PDF greater or equal to the threshold value will use this rule:

$$\left.\begin{array}{c} P\big(T,S\big|\Theta\big)_{SGM} \geq \big(thr\big)_{SGM} \\ OR \\ P\big(T,S\big|\Theta\big)_{GMM} \geq \big(thr\big)_{GMM} \end{array}\right\} \quad \rightarrow \quad \text{Skin pixel} \tag{7}$$
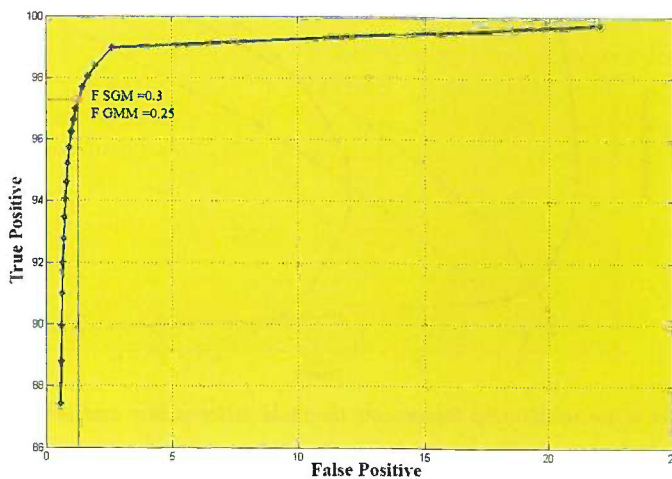
Fig. 6: The ROC of testing image 1

EXPERIMENTAL RESULTS

To test the performance of the proposed method, 45 test images of people from various ethnic groups under various conditions are used. The model performance can be evaluated as how the TP value can be greater and how the FP value can be smaller at the same time. Experiment results show that, when SGM and GMM are used together, TP

value is always greater than TP value in the model based on SGM or GMM being used separately. When SGM and GMM are used together, FP is almost equal to the greater value of FP of SGM or GMM. *Fig. 7* illustrates this observation.
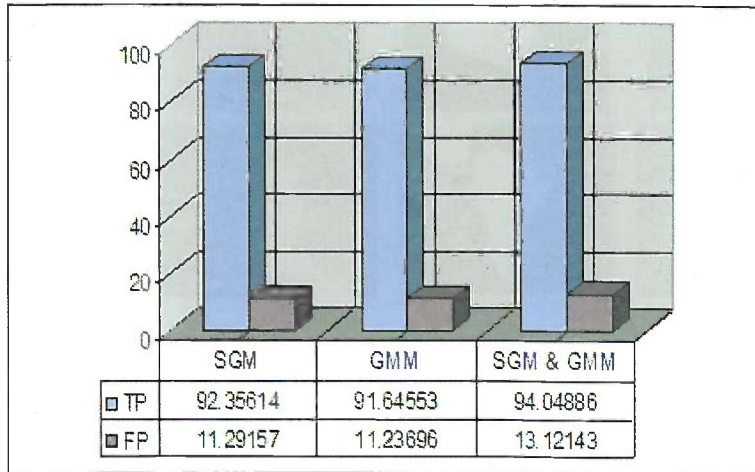

	SGM	GMM	SGM & GMM
□ TP	92.35614	91.64553	94.04886
▣ FP	11.29157	11.23696	13.12143

Fig. 7: Model performance comparisons: SGM, GMM and SGM and GMM

The results show that using a small fixed threshold value leads to increase in the TP and FP, and using great fixed threshold value leads to decrease in the TP and FP. On the other hand, each image has its own environmental conditions such as ambient lights, complex backgrounds and others, where some images can be segmented to skin and non-skin regions perfectly by using a small threshold value, and vice versa. For all these reasons, the adaptive threshold value represents the solution for such problems. *Fig. 8* shows a performance comparison of the model with three kinds of threshold values.

	adaptiv Thresohld	fixed threshold thSGM=1.7879 thGMM=1.2736	fixed threshold thSGM=9.7543 thGMM=10.6493
□ TP	94.04886	96.12707	89.2877
▣ FP	13.12143	19.00266	7.8315
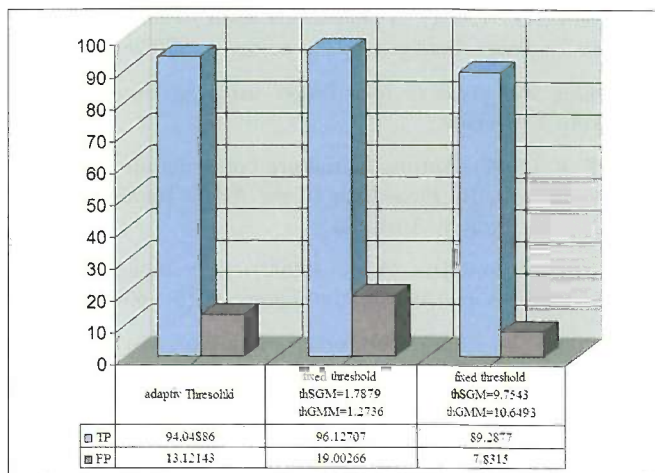
Fig. 8: Model performances with three kinds of threshold values

Fig. 9 shows some test images and their skin map images.

Fig. 9: Some test images and their skin map image

CONCLUSIONS

The suggested model shows an efficiency performance in detecting the human skin in still colour images, apart from the variety of the human races and the complexity of the backgrounds. The SDM performs normally when the image contains shadowed skin, but not to the same degree of accuracy when images contain human skin under bright light conditions. The experimental results show that the average of the accuracy rate of the test images as more than 94%, while the standard deviation is 4.2%.

However, there are several problems with the proposed SDM method. These problems include when the background contains surfaces and objects with skin-like colours. In such cases, the results show that the TP value can be accepted as usual, where the results also show that in such images, the FP rises to 50% and more.

REFERENCES

CAETANO, T. S. and BARONE, D.A.C. (2001). *A probabilistic model for the human skin color.* In *IEEE 11th International Conference on Image Analysis and Processing* (p. 279-283). Palermo, Italy.

GOKALP, D. (2005). *Learning skin pixels in color images using gaussian mixture.* Technical report. Ankara, Turkey: Bilkent University.

GOMEZ, G. and MORALES, E. F. (2002). Automatic feature construction and a simple rule induction algorithm for skin detection. In *Proceedings of the ICML Workshop on Machine Learning in Computer Vision* (p. 31-38). Sydney, Australia.

HSU, R. L., ABDEL-MOTTALEB, M. and JAIN, A. K. (2002). Face detection in color images. *IEEE Transactions on Pattern Analysis and Machine Intelligence,* 24(5), 696-706.

LEE, J. Y. and YOO, S. I. (2002). An elliptical boundary model for skin color detection. In *The 2002 International Conference on Imaging Science, Systems, and Technology.* Las Vegas, USA.

MUKHOPADHYAY, N. (2000). *Probability and Statistical Inference.* New York, USA: Marcel Dekker Inc.

PHUNG, S. L., BOUZERDOUM, A. and CHAI, D. (2005). Skin segmentation using color pixel classification: analysis and comparison. *IEEE Transactions on Pattern Analysis and Machine Intelligence,* 27(1), 148-154.

TERRILLON, J. C., SHIRAZI, M. N., FUKAMACHI, H. and AKAMATSU, S. (2000). Comparative performance of different skin chrominance models and chrominance spaces for the automatic detection of human faces in color images. In *Proceedings of the 4th IEEE International Conference on Automatic Face and Gesture Recognition* (p. 54-61). Grenoble, France.

VEZHNEVETS, V. and ANDREEVA, A. (2005). *A comparative assessment of pixel-based skin detection methods.* Technical report. Moscow, Russia: Graphics and Media Lab., Moscow State University.

VEZHNEVETS, V., SAZONOV V. and ANDREEVA A. (2003). A survey on pixel-based skin color detection techniques. In *Proceedings of the Graphicon* (p. 85-92). Moscow, Russia.

ZARIT, B.D., SUPER, B.J. and QUEK, F.K.H. (1999). Comparison of five color models in skin pixel classification. In *Proceedings of IEEE International Workshop on Recognition, Analysis, and Tracking of Faces and Gestures in Real-Time Systems* (p. 58-63). Corfu, Greece.

ZHU, Q., CHENG, K. T., WU, C. T. and WU, T. L. (2004). Adaptive learning of an accurate skin-color model. In *Proceedings of the Sixth IEEE International Conference on Automatic Face and Gesture Recognition (FGR'04)* (pp. 37- 42). Seoul, Korea.

Relationship between Shear Strength and Soil Water Characteristic Curve of an Unsaturated Granitic Residual Soil

Bujang B.K. Huat[1], Faisal Hj. Ali[2] and S. Hashim[2]
[1]*Department of Civil Engineering, Universiti Putra Malaysia,*
43400 UPM, Serdang, Selangor, Malaysia
[2]*Department of Civil Engineering, University of Malaya,*
Kuala Lumpur, Malaysia
E-mail: bujang@eng.upm.edu.my

ABSTRACT

The three shear strength parameters that are required to define a failure envelope of an unsaturated soil are c' (apparent cohesion), ϕ' (effective angle of friction), and ϕ^b (shear strength change with change in matric suction). A soil-water characteristic curve (SWCC) that relates the water content of a soil to matric suction is another important relationship in unsaturated soil mechanics. The SWCC essentially shows the ability of an unsaturated soil to retain water under various matric suctions. It has a similar role as the consolidation curve of a saturated soil that relates void ratio or water content to effective stress. The SWCC of a soil dictates the manner by which the permeability, shear strength and volume change of the soil will behave at different matric suctions upon drying and wetting. Since water can only flow through the water-filled pores, the SWCC therefore, essentially indicates the space available for the water to flow through the soil at various matric suctions. This paper describes a study on the shear strength-SWCC relationship that was carried out on an unsaturated granitic residual soil. It is observed that the failure envelope of an unsaturated soil is non-linear due to the non-linear soil water characteristic curve (SWCC). At low matric suctions, where the suction is lower than the air-entry value of the soil, the soil is at or near saturation condition and behave as though it is saturated. Consequently an increase in matric suction produces the same increase in shear strength as does an increase in net normal stress. However, at matric suctions higher than the air-entry value of the soil (> 200 kPa), the soil starts to desaturate. The increase in shear strength with respect to matric suction becomes less than the increase with respect to the net normal stress.

Keywords: Matric suction, shear strength, soil water characteristic curve, unsaturated soil mechanics

INTRODUCTION

The microclimatic conditions in an area are the main factors causing the soils to be unsaturated. Therefore, unsaturated soils or soils with negative pore-water pressures can occur in essentially any geological rock type or climatic environment, such as residual soil, a lacustrine deposit, and soils in arid and semi arid areas with deep ground water table. In Malaysia, residual soil over granite and sedimentary rocks occur extensively, i.e. cover more than 80% of the land area. Yet, not much research work has been carried out on these materials. The situation is even worst in the case of unsaturated residual soils.

Tropical residual soils have some unique characteristics related to their composition and the environment in which they develop. Their strength and permeability are likely to be greater than those of temperate zone soils with comparable liquid limits (Ali and Rahardjo, 2004). Most classical concepts related to soil properties and soil behavior have

been developed for temperate zone soils, and there has been difficulty in accurately modeling procedures and conditions to which residual soils are subjected. Engineers appear to be slowly recognizing that residual soils are generally soils with negative in situ pore-water pressures, and that much of the unusual behavior exhibited during laboratory testing is related to a matric suction change in the soil (Fredlund and Rahardjo, 1985, 1993). There is the need for reliable engineering design associated with residual soils (Ali and Rahardjo, 2004).

When the degree of saturation of a soil is greater than about 85%, saturated soil mechanics principles can be applied. However, when the degree of saturation is less than 85%, it becomes necessary to apply unsaturated soil mechanics principles (Fredlund and Rahardjo, 1987). The transfer of theory from saturated soil mechanics to unsaturated soil mechanics and *vice versa* is possible through the use of stress state variables. Stress state variables define the stress condition in a soil and allow the transfer of theory between saturated and unsaturated soil mechanics. The stress state variables for unsaturated soils are net normal stress (σ-u_a) and matric suction (u_a-u_w), where s is the total stress, u_a is the pore-air pressure and u_w is the pore-water pressure. The stress state in an unsaturated soil can be represented by two independent stress tensors as (Fredlund and Morgenstern, 1977):

$$\begin{bmatrix} (\sigma_x - u_a) & \tau_{xy} & \tau_{xz} \\ \tau_{yx} & (\sigma_y - u_a) & \tau_{yz} \\ \tau_{zx} & \tau_{zy} & (\sigma_y - u_a) \end{bmatrix} \tag{1}$$

$$\begin{bmatrix} (u_a - u_w) & 0 & 0 \\ 0 & (u_a - u_w) & 0 \\ 0 & 0 & (u_a - u_w) \end{bmatrix} \tag{2}$$

where, σ_x, σ_y, σ_z in Equation 1 are the total normal stresses in the x-, y-, and z-directions, respectively; and τ_{xy}, τ_{yx}, τ_{xz}, τ_{zx}, τ_{zy} and τ_{yz} are the shear stresses.

In term of shear strength, there are three shear strength parameters that are required to define a failure envelope of an unsaturated soil, which is an extended form of the Mohr-Coulomb equation (Fredlund *et al.*, 1978). They are c' (apparent cohesion), ϕ' (effective angle of friction), and ϕ^b (shear strength change with change in matric suction).

A soil-water characteristic curve (SWCC) that relates the water content of a soil to matric suction is another important relationship for unsaturated soil mechanics. The SWCC essentially shows the ability of an unsaturated soil to retain water under various matric suctions. It has a similar role as the consolidation curve of a saturated soil that relates void ratio or water content to effective stress. The SWCC of a soil dictates the manner in which the permeability, shear strength and volume change of the soil will behave at different matric suctions upon drying and wetting (Fredlund and Rahardjo, 1993). Since water can only flow through the water-filled pores, the SWCC therefore, essentially indicates the space available for the water to flow through the soil at various matric suctions.

This paper describes a study on the shear strength-SWCC relationship that has been carried out on an unsaturated granitic residual soil.

TEST EQUIPMENTS AND MODIFICATION

A series of laboratory direct shear test with fixed suction were performed to see if the modified apparatus is suitable for testing the shear strength of unsaturated residual soils; to see if the results obtained comply with the extended Mohr Coulomb failure criterion of Fredlund and Morgenstern (1977), as well as for comparison with the results of other similar studies on unsaturated residual soils.

Fig. 1 shows an ordinary shear box that has been modified to apply matric suction to the soil samples. Suction is applied by controlling the pore air and pore water pressures. The direct shear box is placed in a special fabricated galvanized steel air chamber as shown in *Fig. 1*. A 15 bar high air entry disc is placed at the lower block of the direct shear box. The high air entry disc is used to separate soil samples with the water compartment underneath.
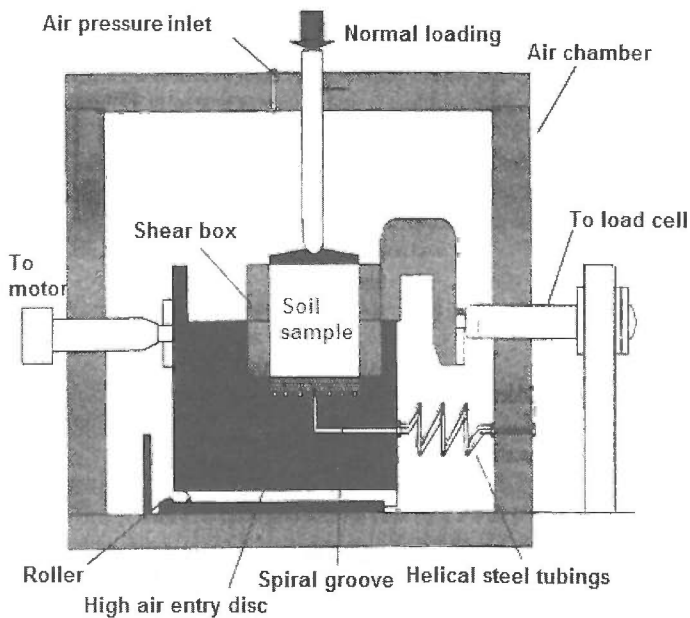
Fig. 1: Modified direct shear apparatus

The total normal stress, σ, is applied vertically to the soil specimen through a loading ram as in the conventional shear box tests. However in this case, the uplift pressure of the air in the air chamber on the loading ram has to be taken into account.

In order to study the soil water characteristic curve of an unsaturated residual soil, the conventional Rowe Cell is modified and used together with the GDS pressure controllers, using the principles of the pressure plate or axis translation technique (Hilf, 1956) for the application of suction. The modification involved removal of the rubber membrane from the cell top, detachment of the side drainage porous layer, blocking of drainage outlet and the fabrication of a completely new base to include the seating for high air-entry ceramic disc and spiral grooved compartment for flushing the diffused air from below the disc, as shown in *Fig. 2*.
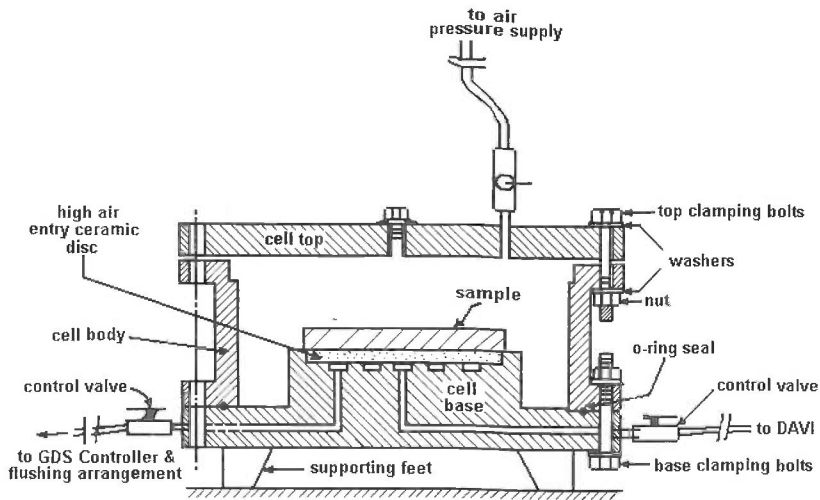
Fig. 2: Modified Rowe cell

The schematic of the test arrangement is shown in *Fig. 3*. The volume of water flowing in or out of the sample is recorded by the GDS pressure controller.
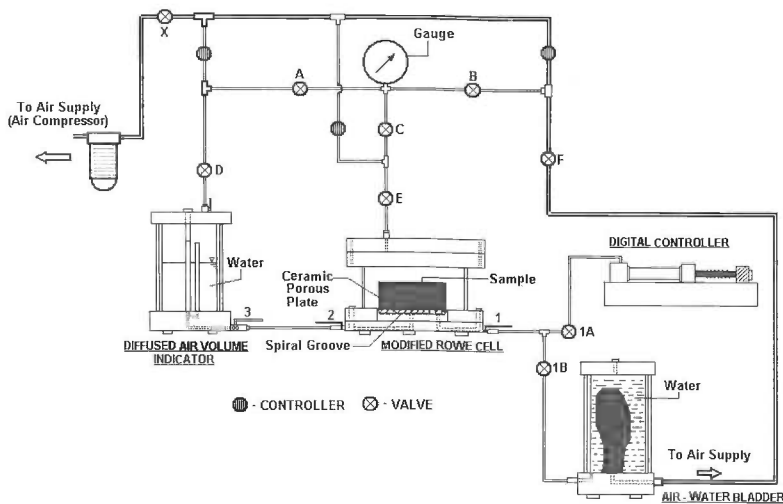

Fig. 3: Schematic arrangement of test setup using modified Rowe cell

SOIL SAMPLE

The soil samples used is this study were obtained from a cut slope at KM 31 of the Kuala Lumpur-Karak Highway. These were residual soils of weathering grade VI, according to the commonly used classification system of Little (1969) that had been formed over porphyritic biotite granite bedrock commonly found in Peninsular Malaysia (Raj, 1985). Table 1 summarizes the basic engineering properties of the soil samples.

TABLE 1
Physical and index properties of the soil sample

Properties	
Weathering grade	VI
Description	Yellowish brown sandy silty clay
Natural water content	22.9 – 27.3%
Liquid limit	95%
Plastic limit	45%
Specific Gravity	2.68
Clay mineral	kaolinite
Particle size distribution:	
Gravel	1.7%
Sand	47%
Silt	11.3%
Clay	40%
Permeability, k	$2.5 – 4.1 \times 10^{-8}$ m/s

Tropical residual soils are usually non homogeneous and anisotrophic, making representative sampling particularly difficult. In this study, block samples measuring 200 x 200 x 200 mm (width x length x height) were collected from the site in metal boxes. These were then cut to the sample sizes in the laboratory.

RESULTS AND DISCUSSION

Fig. 4 show plot of failure envelope with respect to net normal stress plane $(\sigma_n - u_a)$ obtained from the direct shear test with fixed suction ranging from 50 to 350 kPa. The soil effective angle of friction ø' is found to range from 20.3° to 29.9° with an average ø' angle of 24.6° (ø' ≈ 25°).
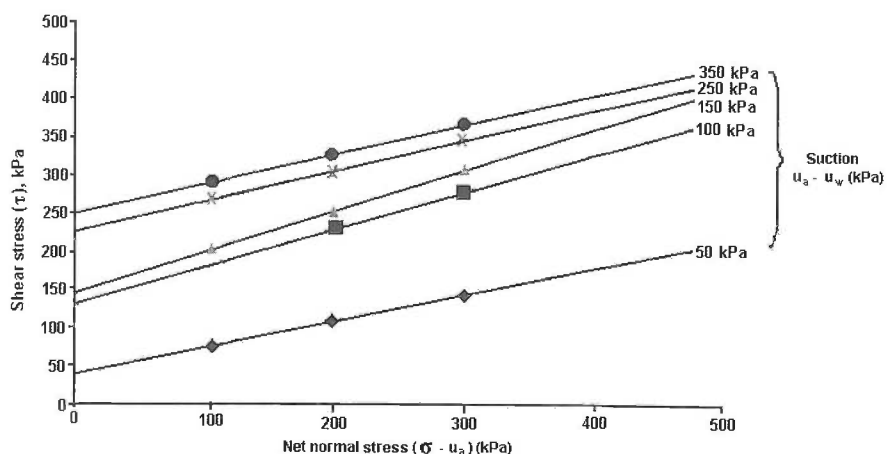
Fig. 4: Failure envelopes with respect to net normal stress, $(\sigma - u_a)$ for test with fixed suction

Theoretically ø' should not vary too much (Fredlund *et al.*, 1978). In other words the lines for different values of suction, $(u_a\text{-}u_w)$, should be roughly parallel. However, Escario and Saez (1986), Gan and Fredlund (1988) and Abdullah *et al.* (1994) in their research found that the lines showed a tendency for slight divergence at increasing loads, which appears to be in agreement with this study.

This certainly proves that soil suction does play a role towards increasing the shear strength of a soil, and also verifies the unsaturated soil mechanics theory (Fredlund and Morgenstern, 1977; Fredlund *et al.*, 1978: Fredlund and Rahardjo, 1993).

Fig. 5 shows of failure envelope with respect to the matric suction $(u_a - u_w)$ plane. Also plotted is the soil water characteristic curve (SWCC). The non-linearity of the failure envelope of unsaturated soil as reported by earlier studies (Escario and Saez, 1986; Gan and Fredlund, 1988; Abdullah *et al.*, 1994) is evident in this plot. This is due to the non-linear soil water characteristic curve (*Fig. 5a*).

At low matric suctions, where the suction is lower than the air-entry value of the soil, the soil is at or near saturation condition and the air phase consists of a few occluded bubbles (Corey, 1957). The soil would be expected to behave as though it was saturated. In other words the negative pore-water pressure acts throughout the predominantly water filled pores as in the saturated soil condition. Consequently an increase in matric suction produces the same increase in shear strength as does an increase in net normal stress. As a result, the same values are obtained for ϕ' and ϕ^b. ϕ^b is defined as change in shear strength with change in suction, that is the angle of the second portion of the failure envelopes.
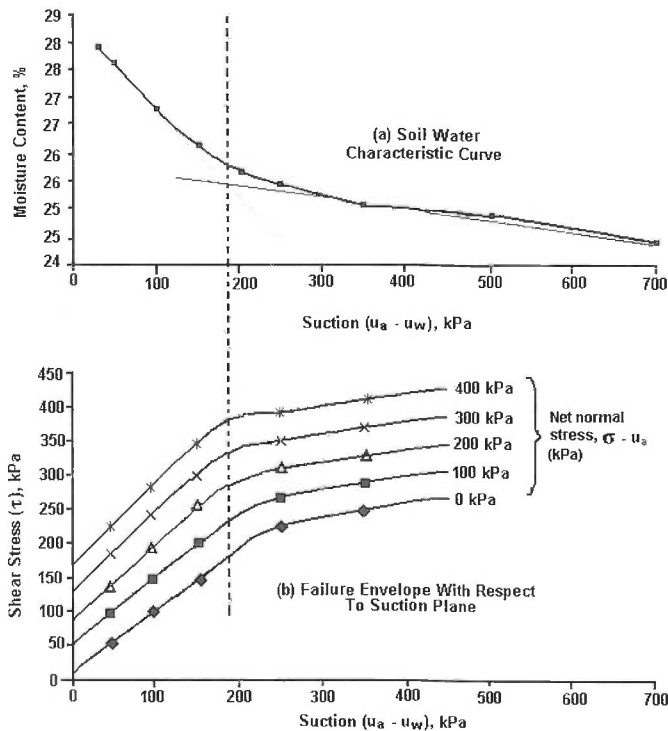
Fig. 5: Relationship between soil-water characteristic curve and shear strength

At matric suctions higher than the air-entry value of the soil (approximately > 200 kPa), the soil starts to desaturate. The negative pore-water pressure does not act throughout the entire pores as in the saturated soil condition. Therefore, the contribution of matric suction towards the strength of the soil is less than the contribution of the net normal stress at the same stress level. In other words the increase in shear strength with respect to matric suction is less than the increase with respect to net normal stress. As a result, the ϕ^b value becomes less than ϕ' at high matric suctions as observed in *Fig. 5*. The value of ϕ^b obtained is the range of 11.6 to 13.1° which an average value of 12, which is much less than the value ϕ' ($\phi' \approx 25°$).

CONCLUSIONS

From the results of this study, the following conclusion can de drawn with regards to the shear strength, matric suction and soil water characteristics curve (SWCC) of unsaturated residual soil.

Soil suction does play a role towards increasing the shear strength of an unsaturated soil.

The non-linearity of the failure envelope of unsaturated soil is due to the due to the non-linear soil water characteristic curve (SWCC).

At low matric suctions, where the suction is lower than the air-entry value of the soil, the soil is at or near saturation condition and behave as though it was saturated. Consequently an increase in matric suction produces the same increase in shear strength as does an increase in net normal stress.

At matric suctions higher than the air-entry value of the soil (> 200 kPa), the soil starts to desaturate. The increase in shear strength with respect to matric suction is then becomes less than the increase with respect to the net normal stress.

REFERENCES

ABDULLAH, A., ALI, F. and CHANDRASEGARAN. (1994). Triaxial shear strength tests on partially saturated residual soils. *Geotropika.* Malacca.

ALI, F.H. and RAHARDJO, H. (2004). Unsaturated residual soil. In Huat *et al.* (Ed.), *Tropical residual soils engineering* (p. 57-71). Leiden. Balkema.

COREY, A.T. (1957). Measurement of water and air permeability in unsaturated soils. *Proceedings of the Soil Science Society of America, 21*(1), 7-10.

ESCARIO, V. and SAEZ, J. (1986). The shear strength of partially saturated soils. *Geotechnique, 36*(3), 436-436.

FREDLUND, D.G. and MORGENSTERN, N.R. (1977). Stress state variables for unsaturated soils. *J. of the Geotechnical Engineering Division, ASCE, 103,* 447-466.

FREDLUND, D.G., MORGENSTERN, N.R. and WIDGER, R.A. (1978). The shear strength of unsaturated soils. *Canadian Geotechnical Journal, 15*(3), 313 – 321.

FREDLUND, D.G. and RAHARDJO, H. (1985). Theoretical context for understanding unsaturated residual soils behavior. In *Proceeding 1ˢᵗ International Conference Geomech. in Tropical Laterite and Saprolitic Soils* (p. 295-306). Sao Paolo, Brazil.

FREDLUND, D.G. and RAHARDJO, H. (1987). Soil mechanics principles for highway engineering in Arid regions. In soil mechanics considerations: Arid and semiarid areas. *Transportation Research Record, 1137,* 1-11.

FREDLUND, D.G. and RAHARDJO, H. (1993). *Soil Mechanics for Unsaturated Soil.* New York: John Wiley & Sons.

GAN, J.K.M. and FREDLUND, D.G. (1988). Determination of shear strength parameters of an unsaturated soil using the direct shear box. *Canadian Geotechnical Journal, 25,* 500-510.

HILF, J.W. (1956). *An investigation of pore pressure in cohesive soils.* US Bureau of Reclamation, Technical Memorandum. No. 654.

LITTLE, A.L. (1969). The engineering classification of residual tropical soils. In *Proc. 7th International Conference Soil Mechanics Foundation Engineering (1,* 1-10). Mexico.

RAJ, J.K. (1985). Characterization of the weathering profile developed over porphyritic biotite granite in Peninsular Malaysia. *Bulletin of the International Association of Engineering Geology, 32,* 121-127. Paris.

Extending the Range of an Optical Vanadium(V) Sensor Based on Immobilized Fatty Hydroxamic Acid in Poly (Methyl Methacrylate) Using Artificial Neural Network

Azizul Isha[1], Nor Azah Yusof[2], Musa Ahmad[3], Dedy Suhendra[2], Wan Md. Zin Wan Yunus[2] and Zulkarnain Zainal[2]

[1]*Department of Chemistry, Faculty of Science, Universiti Malaya,
50603 Kuala Lumpur, Malaysia*
[2]*Department of Chemistry, Faculty of Science, Universiti Putra Malaysia,
43400 UPM Serdang, Selangor, Malaysia*
[3]*School of Chemical Sciences and Food Technology,
Faculty of Science and Technology, Universiti Kebangsaan Malaysia,
43600 Bangi, Selangor, Malaysia*

ABSTRACT

An artificial neural network (ANN) was applied for the determination of V(V) based on immobilized fatty hydroxamic acid (FHA) in poly(methyl methacrylate) (PMMA). Spectra obtained from the V(V)-FHA complex at single wavelengths was used as the input data for the ANN. The V(V)-FHA complex shows a limited linear dynamic range of V(V) concentration of 10 - 100 mg/L. After training with ANN, the linear dynamic range was extended with low calibration error. A three layer feed forward neural network using back-propagation (BP) algorithm was employed in this study. The input layer consisted of single neurons, 30 neurons in hidden a layer and one output neuron was found appropriate for the multivariate calibration used. The network were trained up to 10 000 epochs with 0.003 % learning rate. This reagent also provided a good analytical performance with reproducibility characters of the method yielding relative standard deviation (RSD) of 9.29% and 7.09% for V(V) at concentrations of 50 mg/L and 200 mg/L, respectively. The limit of detection of the method was 8.4 mg/L.

Keywords: Artificial neural network (ANN), V(V), fatty hydroxamic acid (FHA), poly(methyl methacrylate) (PMMA)

INTRODUCTION

Optical sensors have become major analytical tools in monitoring the nature of chemical in the environment. Optical sensors, often called "optodes", are a particular type of chemical sensor where spectroscopic measurements associated with chemical reactions are carried out (Guell *et al.*, 2007). Optical sensor based on the use of uv-visible spectrophotometry for the determination of V(V) was developed and PMMA membrane was applied as supporting material in this study. FHA was used as a new reagent for the determination of V(V) and showed good properties in our preliminary study using a manual batch method (Isha *et al.*, 2003).

The FHA was synthesized by reacting hydroxylamine with refined, bleached deodorized (RBD) palm kernel olein (liquid phase from the fractionation of palm kernel oil) using lipase as biocatalyst. FHA is produced with glycerol as a bi-product (Suhendra, 2002). *Fig. 1* shows the preparation reaction for FHA. The transfer of acyl group from a donor ester to hydroxylamine (aminolysis) was catalyzed preferentially by the reaction of free fatty

acids. The exact structure and the molecular weight of FHA have not yet been determined. The suggested complex formation structure of V(V)-FHA complex is shown in *Fig. 2*. FHA is a white colour solid and colourless when in liquid form. FHA is slightly soluble in alcohol but not soluble in water.
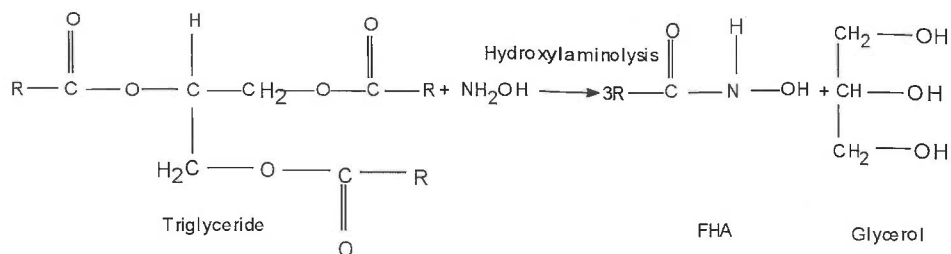
Where R is a mixture of following fatty acid chain: caproic acid, caprylic acid, capric acid, lauric acid, myristic acid, palmitic acid, oleic acid and linoleic acid.
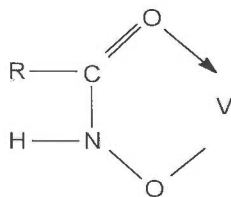
Fig. 1: Preparation reaction for FHA

Fig. 2: Structure of V(V)-FHA complex

The need for V(V) analysis in environmental analysis has increased after a report on the different biological roles of ionic forms of this species in plants, animals and humans. Human exposure to vanadium has severe effects on cell growth, cardiac muscle, diuretic kidney function (Gavasov, 2000) and symptoms such as nervous depression, coughing, vomiting, anemia and increased risk of lung cancer, that are sometimes fatal (Ahmad and Banoo, 1999). The neurotoxicity of vanadium can cause somnolence, convulsions, respiratory failure and gastrointestinal irritation with diarrhea (Faulkner-Hudson, 1964).

PMMA membrane immobilized FHA determine the V(V) in limited linear dynamic range. Therefore, a good approach must be taken to extend the response range of this optical sensor. ANN was found to be a suitable program to solve this problem. Taib *et al.* (1996) first introduced the use of ANN as the mechanism to modelling complex non-linear data, applications of ANN in optical fibre chemical sensor technology.

Generally, ANN is a system loosely modelled on the human brain. It represents an important paradigm for classifying patterns or approximating complex non-linear process dynamics. These properties clearly indicate that neural network exhibit some intelligent behaviour, and are good candidate models for non-linear processes, for which no perfect mathematical model is available (Denai *et al.*, 2007). It is an attempt to simulate within specialized hardware, the multiple layers of simple processing elements called neurons. Each neuron is linked to certain of its neighbours with varying coefficients of connectivity that represent the strengths of these connections (Gonzalez and Dankel, 1993; Zahedi, 1993; Simon, 1994). ANN has to be trained. This means that, given a set of input-output

patterns (called the training set), the connection weights of the neural network are adjusted in order to approximate the input-output patterns provided in the training set according to some predefined criterion. After training, the neural network can be used to predict a new output pattern, based on the input pattern only. The adaptation law that allows adjusting the connection weights is called the learning algorithm (Denai *et al.*, 2007).

The aim of this study is based on the application of ANN to extend the useful linear range in the determination of V(V) ion based on immobilized FHA in PMMA. ANN with feed-forward network having a single hidden layer and the back-propagation algorithm was applied in this work.

EXPERIMENTAL

Reagent

All chemicals used were of analytical grade and deionized water was used throughout for solution preparation. A stock solution (5.0 x 103 mg/L) of V(V) was prepared by dissolving 0.5 g of V2O5 (BDH) in 100 mL of 1.0 M HCl (Merck). Working standard solution of V(V) were prepared by appropriate dilution of the stock solution before use.
Synthesis of FHA

Hydroxylamine hydrochloride (Fischer), sodium hydroxide (J.T Baker) and crude palm kernel olein (Southern Edible Oil) in hexane (J.T. Baker) were reacted in the presence of Lipozyme (Novo Nordisk). The lypozyme used were able to catalyze hydroxylaminolysis reaction which shows the highest activity. This is probably because lipozyme is an immobilized lipase, which has more storage stability and more active lipase than native and modified lipases, and its presence at the interface of the system with others at the bottom of the water phases evokes the contact of all the components in the lypozyme system better than others. The reaction was carried out in a sealed glass flask in water shaker bath with continuous shaking. The Lipozyme was separated by a filter paper and the yield was dried. The products were purified by crystallization in hexane and dried.

Reagent Immobilization

The doped PMMA membrane was prepared by adding 0.7006 g of dry PMMA powder and 0.0405 g of FHA into 10 mL of tetrahydrofuran. Then 210 _L of tributyl phosphate was added into the mixture. The solution was mixed thoroughly and poured into a petri dish with a diameter of 10 cm. The mixture was left to dry overnight to enable a smooth and even membrane to form. The membrane was cut into1.0 cm x 4.0 cm size.

Procedure

The membrane was placed vertically inside a plastic cuvette. The absorption spectra of PMMA immobilized FHA alone and the complex formation between PMMA immobilized FHA and 100 mg/L was recorded at wavelength 350 to 700 nm. The absorbance was measured five minutes after placement of the membrane in the V(V) solution.

The dynamic range was studied by placing the PMMA membrane in different concentrations of V(V) solution, i.e. 1 - 110 mg/L. The absorbance was measured at a wavelength of 495 nm.

The reproducibility was studied at V(V) concentration of 50 ppm and 200 ppm. A total of ten different batches of similarly prepared membranes were immersed in the

same concentration of analyte solution. In this study, two different concentrations of V(V) solution were used, i.e. 10 mg/L and 200 mg/L. The absorbance was measured and the relative standard deviation in the measurement was calculated.

INSTRUMENTATION

Spectral measurements were made with an ultraviolet-visible spectrophotometer (Varian-Cary Win UV 100). For each concentration, the spectrum was scanned at wavelengths of 350 - 750 nm. A total of 20 spectral readings were obtained. Five of these spectra (V(V) concentrations of 31, 39, 46, 52 and 108 mg/L) were used for testing the trained network whilst the remaining spectra (10, 40, 50, 55, 60, 65, 70, 75, 80, 85, 90, 95, 100, 105 and 110 mg/L) were used for training the network.

DATA TREATMENT AND ANALYSIS

A feed-forward ANN having a single hidden neuron layer with back-propagation (BP) training algorithm was employed for treatment of the data. The input layer consists of single neurons, which represent the absorbance intensities measured at one wavelength from each spectrum. The output layer consists of a single neuron which represents the concentration value of V(V). A network having up to 40 neurons in hidden layer, was considered in this study.

The network training and data treatment were realized by using Matlab program (Matlab, 2004) under an Intel Celeron processor having 256 MB of RAM. The training and optimization process carried out in this study is shown in Table 1. The network was trained up to 10 000 epochs and the progress of the sum-squared error (SSE) between the calculated and the measured output was recorded. Finally, a new set of input data was introduced to the networks to check for prediction capability and precision.

TABLE 1
The general setting of the back-propagation specific parameters during network training

Specific Parameters	Values
Maximum number of epochs to train	10 000
Sum-squared error (SSE) goal	0.02
Learning rate	0.003
Frequency of progress displays (in epochs)	500

The preference of the best network was based on several tests using the trained network that incorporates the inspection for training data fitting errors and prediction test of errors. The selected network was then applied for computer generated application where new measurements were taken, processed and converted to concentration values employed by the Matlab program simulation.

RESULTS

Spectral Studies
Fig. 3 shows the absorbance spectra of the immobilized FHA pre and post reaction with V(V). The formation of the complex causes an increase in absorbance due to a change

in color of the membrane from colorless to dark purple. The maximum absorbance difference of the two absorbance spectra was observed at 495 nm and this wavelength was therefore used for further measurements.

THE DYNAMIC RANGE OF THE V(V) CONCENTRATION

The typical analytical curve of the sensor response as a function of V(V) concentration is shown in *Fig. 4*. It shows that the sensing material produced a linear response when the V(V) concentration is within the range of 10 - 100 ppm. The limit of detection was calculated to be 8.4 ppm. According to IUPAC definition, the limit of detection has defined as the concentration that produces a signal that exceeds the signal observed from a blank by an amount equal to three times the standard deviation for the measurement on the blank.
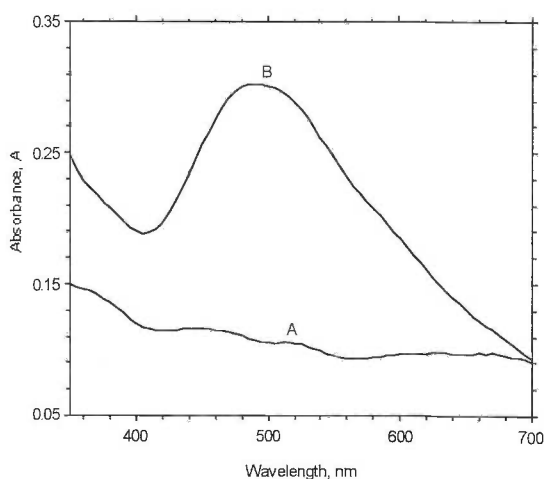
Fig. 3: Absorbance spectra of PMMA immobilized FHA before (A) and after (B) reaction with 100 ppm V(V)
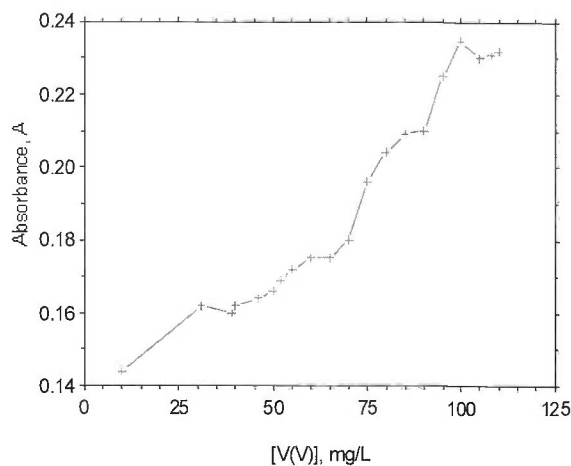
Fig. 4: The response curve of the PMMA immobilized FHA towards different concentrations of V(V)

Multivariate Calibration Using ANN

Data obtained from uv-visible spectrophotometer were used as input to the ANN. Single wavelength point (459 nm) from each spectrum was chosen to represent the input data for the ANN to avoid several problems during network training periods (Garg and Bozink, 1972; Bos *et al.*, 1993). The points selected, were due to their significant variations in the sensor signal.

Fifteen spectra were used for the training of the ANN. Network optimization was performed by changing the number of neurons in the hidden layer, the number of cycles during training and the percentage of learning rate. Table 2 shows the SSE values of the network with 5, 10, 15, 20, 25, 30, 35 and 40 neurons in hidden layer after completing the 10 000 epochs.

TABLE 2
SSE values obtained from the networks consists of neurons in
hidden layer after being trained with 10 000 epochs

Number of neuron in hidden layer	Sum-square error (SSE)
5	194.5040000
10	56.1151000
15	128.5680000
20	3.9953800
25	0.5797560
30	0.0199902
35	0.0199961
40	0.0199976

For the network with five neurons in hidden layer, the convergence of SSE was observed to be very slow. The fastest convergence of SSE was achieved using 30 neurons in the hidden layer. The number of hidden neurons when arranged in declining SSE order was 5, 15, 10, 20, 25, 40, 35 and 30. Network trained with 10 000 epochs were suitable to be used in predicting the response of the concentration of V(V) since it showed a low SSE value. Zupan and Gasteiger (1991) reported that, ANN training by using much higher number of epochs usually caused problems such as over training and over fitting problems. Five calibration spectra (31, 39, 46, 52 and 108 mg/L) were employed to establish their prediction capability. The trained networks with different number of hidden neurons were present to improve the process in choosing the best network's architecture (Bos *et al.*, 1993; Taib and Narayanaswamy, 1997).

Different values of learning rate (0.0070 - 0.0001) from the networks consists 30 neurons in hidden layer after observation. As shown in Table 3, a learning rate of 0.0030 gave the lowest SSE value followed by 0.005, 0010, 0.0005, 0.0003, 0.0070 and 0.0001.

Table 4 shows the predicted concentration values against the expected concentration values measured using a uv-visible spectrophotometer. As shown in Table 4, the network with 20, 25 and 30 neurons in the hidden layer produced good predictions with average calibration errors of 0.5197, 0.7586 and 0.5185, respectively. *Fig. 5* shows the fitted training data and calibration by the network with 30 neurons in the hidden layer.

TABLE 3
SSE values obtained from the networks consists 30 neurons in hidden layer
after being trained with 10 000 epochs in different value of learning rate

Learning rate	Sum-square error (SSE)
0.0001	120.8410000
0.0003	2.0346600
0.0005	1.1228000
0.0010	0.9130860
0.0030	0.0199902
0.0050	0.0714400
0.0070	6.4872000
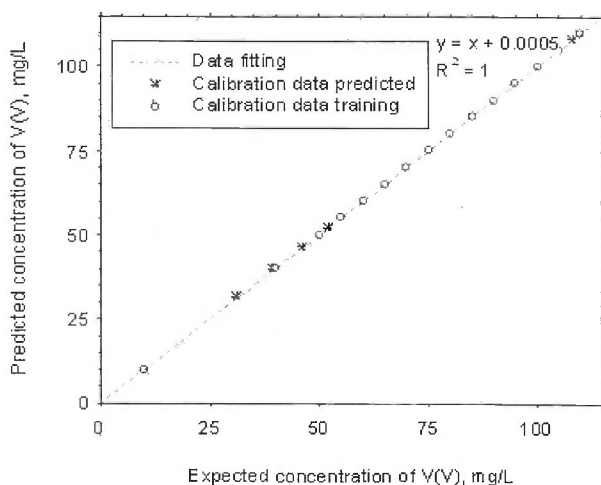
Fig. 5: *Training data fitting and calibration by the network with 30 neurons in the hidden layer*

It was found that, the network with 30 neurons in hidden layer gave the best architecture for generating accurate prediction of V(V) concentration. This network extends the useful response range of the PMMA immobilized FHA in determination of V(V) above 100 mg/L.

Reproducibility Study

Reproducibility refers to the discrepancies in response between individual members of a batch of similar preparation membrane (Yusof and Ahmad, 2002). The results indicate that the developed method is reproducible when used for measurements of V(V) at concentrations of 50 mg/L and 200 mg/L. The relative standard deviations were calculated to be 9.29% and 7.09% for 50 mg/L and 200 mg/L of V(V), respectively.

The variation in the determination of V(V) ion using this sensing membrane was due mainly to variation during preparation of the membrane itself which include variation caused by amount of immobilized reagent. Ahmad and Narayanaswamy (2002) reported similar observations in their reproducibility study of the probe in determination of Al(III) ion.

TABLE 4

The network of V(V) concentration using calibration data

Number of neurons in hidden layer	Expected 31		Expected 39		Expected 46		Expected 52		Expected 108		Average calibration error[a]
	Predicted	Error	Predicted	Error	Predicted	Error	Predicted	Error	Predicted	Error	
5	33.5498	2.5498	38.0757	0.9243	42.1415	3.8585	50.1143	1.8857	102.6810	5.3190	2.9075
10	35.8367	4.8367	40.7900	1.7900	45.2066	0.7934	52.4970	0.4970	108.1285	0.1285	1.6091
15	32.3317	1.3317	40.0098	1.0098	46.2469	0.2469	52.6766	0.6766	102.6649	5.3351	1.7200
20	31.7871	0.7871	40.0059	1.0059	46.5330	0.5330	52.1027	0.1027	108.1696	0.1696	0.5197
25	32.8944	1.8944	40.0000	1.0000	46.0542	0.0542	52.5926	0.5926	108.2519	0.2519	0.7586
30	31.7871	0.7871	40.0000	1.0000	46.5330	0.5330	52.1027	0.1027	108.1696	0.1696	0.5185
35	36.9266	5.9266	40.0000	1.0000	46.0349	0.0349	51.2099	0.7901	108.3622	0.3622	1.6228
40	34.0468	3.0468	40.0000	1.0000	44.8721	1.1279	52.5474	0.5474	108.3072	0.3072	1.2059

[a]Average calibration error $= \sum_{i=1}^{5}$ |predicted V(V) concentration - expected V(V) concentration|/5

CONCLUSION

ANN trained with Back Propagation (BP) algorithm in the highly non-linear calibration of dynamic range of V(V) was successfully performed in this study. A network architecture consisting of single input neurons, 30 neurons in hidden layer and one output neuron after completing the 10 000 epochs with 0.003% learning rate was found appropriate for the multivariate calibration used.

ACKNOWLEDGEMENTS

REFERENCES

AHMAD, M. and NARAYANASWAMY, R. (2002). Optical fibre Al(III) sensor based on solid surface fluorescence measurement. *Sensors and Actuators B*, 81, 259-266.

AHMAD, M.J. and BANOO, S. (1999). Spectrophotometric method for determination of vanadium and its application to industrial, environmental, biological and soil samples. *Talanta*, 48, 1085-1094.

BOS, M., BOS, A. and VAN DE LINDEN, W.E. (1993). Data processing by neural networks in quantitative chemical analysis. *Analyst.*, 118, 323-328.

DENAI, M.A., PALIS, F. and ZEGHBIB, A. (2007). Modeling and control of non-linear systems using soft computing techniques. *Applied Soft Computing*, 7(3), 728-738.

FAULKNER-HUDSON, T.G. (1964). *Vanadium: Toxicology and Biological Significance*. New York: Elsevier.

GARG, D.P. and BOZINK, J.S. (1972). Parameter estimation of non-linear dynamical systems. *Int. J. Control.*, 15, 1121-1127.

GAVASOV, K., SIMEONOVA, ZH. and ALEXANDROV, A. (2000). Extraction spectrophotometric determination of vanadium in natural water and aluminium alloys using PAR and iodo-nitro-tetrazolium chloride. *Talanta*, 52, 539-544.

GONZALEZ, A.J. and DANKEL, D.D. (1993). *The Engineering of Knowledge-based Systems*. Prentice Hall.

GUELL, R., FONTAS, C. and SALVADO, V. (2007). Development of a selective optical sensor for Cr(VI) monitoring in polluted waters. *Analytica Chimica Acta*, 594(2), 162-168.

ISHA, A., YUSOF, N.A., AHMAD, M., SUHENDRA, D. and WAN YUNUS, W.M.Z. (2003). Spectrophotometric determination of trace vanadium (V) ion based on potential fatty hydroxamic acid. *Journal of Physical Science*, 14, 101-111.

MATLAB. (2004). *Rapid data. The MathWorks Inc.* UK: Worthing.

SIMON, H. (1994). *Neural Networks: A Comprehensive Foundation*. New York: MacMillan College Publishing Company.

SUHENDRA, D. (2002). Enzymatic synthesis characterization and application of fatty hydroxamic acid from palm oil. (Ph.D. Thesis, Universiti Putra Malaysia, Serdang, Selangor, 2002).

TAIB, M.N. and NARAYANASWAMY, R. (1997). Multichannel calibration technique for optical-fibre chemical sensor using artificial neural network. *Sensors and Actuators B*, 38-39, 365-370.

TAIB, M.N., ANDRES, R. and NARAYANASWAMY, R. (1996). Extending the range of an optical fibre pH sensor using an artificial neural network. *Anal. Chim. Acta.*, 330, 31-40.

Azizul Isha, Nor Azah Yusof, Musa Ahmad, Dedy Suhendra, Wan Md. Zin Wan Yunus and Zulkarnain Zainal

YUSOF, N.A. and AHMAD, M. (2002). A flow cell optosensor for determination of Co(II) based on immobilized 2-(4-pyridylazo)resorcinol in chitosan membrane by using stopped flow injection analysis. *Sensors and Actuators B, 86,* 127-133.

ZAHEDI, F. (1993). *Intelligence Systems for Business: Expert Systems with Neural Networks.* Wodsworth Publishing Inc.

ZUPAN, J. and GASTEIGER, J. (1991). Neural network: A new method for solving chemical problems or just a passing phase. *Anal. Chim. Acta, 248,* 1-30.

Pixel-Based Skin Colour Detection Techniques Evaluation

**Ahmed M. Mharib[1], Mohammad Hamiruce Marhaban[2]
and Abdul Rahman Ramli[1]**

*Departments of [1]Computer and Communication Systems Engineering
[2]Electrical and Electronic Engineering
Faculty of Engineering, Universiti Putra Malaysia,
43400 UPM, Serdang, Selangor, Malaysia
E-mail: ahmad_muhseen@yahoo.com*

ABSTRACT

Skin detection has gained popularity and importance in the computer vision community. It is an essential step for important vision tasks such as the detection, tracking and recognition of face, segmentation of hand for gesture analysis, person identification, as well as video surveillance and filtering of objectionable web images. All these applications are based on the assumption that the regions of the human skin are already located. In the recent past, numerous techniques for skin colour modeling and recognition have been proposed. The aims of this paper are to compile the published pixel-based skin colour detection techniques to describe their key concepts and try to find out and summarize their advantages, disadvantages and characteristic features.

Keywords: Skin colour detection, computer vision community, pixel - based methods

INTRODUCTION

Skin segmentation is a computer vision process that aims to locate the skin regions in an input image. In the pixel-based skin detection methods, the task can be considered as a standard two-class classification problem; taking each pixel of the input image and producing binary output image that represents both the skin pixel and non-skin pixel. Methods that take pixels spatial relationship into account use the pixel-based method for one of the stages of their algorithms, so they are also at least partially dependant on the performance of the pixel-based methods (Vezhnevets and Andreeva, 2005; Vezhnevets *et al.,* 2003).

The focus will be on the pixel-based methods which in general can be classified into three categories (Gomez and Morales, 2002; Lee and Yoo, 2002; Terrillon *et al.,* 2000; Vezhnevets and Andreeva, 2005; Vezhnevets *et al.,* 2003; Zarit *et al.,* 1999):
- Explicitly defined skin region.
- Nonparametric skin distribution modeling.
- Parametric skin distribution modeling.

HUMAN SKIN COLOUR CHARACTERIZATION

The term "skin colour" is not a physical property of an object, but it is rather a perceptual phenomenon and therefore a subjective human concept. Colour is a perceptual representation of the surface reflectance of an object, as a result of the human eye's sensitivity to electromagnetic radiation wavelengths. Therefore, colour representation similar to the colour sensitivity of the human vision system should help to obtain high performance of the skin detection algorithm (Acharya and Ray, 2005).

Ahmed M. Mharib, Mohammad Hamiruce Marhaban and Abdul Rahman Ramli

Detecting human skin using colour as a feature has several problems. First, the colour representation of a skin obtained by a camera is influenced by many factors such as light and shadow. Second, different cameras produce significantly different colour values even for the same person under the same light conditions. In addition to these, human skin colours differ from one person to another (Jayaram *et al.*, 2004).

COLOUR SPACE REPRESENTATIONS

A wide variety of colour spaces have been applied to the problem of skin colour modeling. Different skin detection methods use different colour spaces. Albiolt *et al.* (2001) showed that for RGB, YCbCr and HSV colour spaces; there exists an optimum skin detector scheme such that the performance of all the skin detector schemes is the same and the separability of the skin and non-skin classes is independent of the colour space chosen.

Jayaram *et al.* (2004) presented an evaluation study of the effect of the pixel colour transformation from the RGB colour space to a non-RGB colour space and the dropping luminance component of the skin colour. The results revealed in the research can be summarized as follows:
1. The improvement in performance due to the colour space transformation was present, but not consistent.
2. The absence of the luminance component decreases performance.
3. The skin colour modeling has a greater impact than the colour space transformation.

EXPLICITLY DEFINED SKIN REGION

A method to build a skin classifier is to define explicitly (through a number of rules) the boundaries skin cluster in some colour spaces. The simplicity of this method has attracted many researchers (Garcia *et al.*, 1999; Gomez and Morales, 2002; Peer *et al.*, 2003; Wimmer and Radig, 2005). Ahlberg (1999) used a simple Discriminates for Face Localization and Facial Feature Extraction to extract skin regions in the image. This method uses the chrominance components of the YCbCr colour space, and the discriminate is as below:

$$\left. \begin{array}{l} 138 < Cr < 178 \\ AND \\ 200 < (Cb + 0.6Cr) < 215 \end{array} \right\} \Rightarrow Skin\,pixel \tag{1}$$

Where Cb and Cr are the blue and red chroma components.

NON-PARAMETRIC SKIN DISTRIBUTION MODELLING

The non-parametric skin modelling methods are used to estimate the skin colour distribution from the training data without deriving an explicit model of the skin colour.

Normalized Lookup Table

There are two issues that must be addressed in building a colour histogram model; the choice of colour space and the size of the histogram which is measured by the number

of bins per colour channel. The colour space is quantized into a number of bins, each of which corresponds to a particular range of colour component value pairs (in 2D case) or triads (in 3D case). These bins, forming 2D or 3D histograms are referred to as the lookup table (LUT). Each bin stores the occurring times of the particular colour in the training skin images. After training, the histogram counts are normalized, converting histogram values to discrete probability distribution (Vezhnevets and Andreeva, 2005).

$$Pskin \ (c) = \frac{skin \ (c)}{Norm} \tag{2}$$

Where $skin(c)$ gives the value of the histogram bin, corresponding to colour vector c and $Norm$ is the normalization coefficient (sum of all histogram bin values, or maximum bin value present). The normalized values of the lookup table bins constitute the likelihood that the corresponding colours will correspond to skin.

To perform skin detection, an image is first transformed into the used colour spaces of LUT. For each pixel in the image, the colour values index the normalized value in the LUT. If this value is greater than a threshold, the pixel is identified as skin. Otherwise, the pixel is considered to be non-skin (Zarit *et al.*, 1999).

Bayes' Classifier

In contrast with the lookup table method, the Bayesian method uses two colour histograms, one for the skin and the other for the non-skin pixels. The probability distribution value, $Pskin(c)$, is actually a conditional probability $P(c|skin)$ "a probability of observing colour c, knowing that we see a skin pixel". A more appropriate measure for skin detection would be $P \ (skin|c)$ "a probability of observing skin, given a concrete c colour value". To compute this probability, the Bayes' rule is used (Vezhnevets *et al.*, 2003):

$$Pskin \ (c) = \frac{P\big(c|skin\big)P\big(skin\big)}{P\big(c|skin\big)P\big(skin\big) + P\big(c|\overline{skin}\big)P\big(c|\overline{skin}\big)} \tag{3}$$

$P(c|skin)$ and $P(c|\overline{skin})$ are directly computed from the skin and non-skin colour histograms equation [2]. The prior probabilities $P(skin)$ and $P(c|\overline{skin})$ can also be estimated from the overall number of skin and non-skin samples in the training set. An inequality $P(c|skin) \geq \Theta$, where Θ is a threshold value, can be used as a skin detection rule.

PARAMETRIC SKIN DISTRIBUTION MODELING

The parametric statistical approaches represent the skin-colour distribution in the parametric form, such as the Gaussian mode. However, the skin-colour distribution is usually multimodal and cannot adequately be represented as a single Gaussian in the colour space. Therefore, the use of a Gaussian mixture model has been proposed. Typically, the Expectation-Maximization (EM) algorithm is employed to fit and update these models based on the observed data (Phung *et al.*, 2005).

Ahmed M. Mharib, Mohammad Hamiruce Marhaban and Abdul Rahman Ramli

Single Gaussian Modeling (SGM)

A Gaussian or normal distribution is a symmetrical frequency distribution having a precise mathematical formula relating the mean and standard deviation of the samples. Gaussian distributions yield bell shaped frequency curves having a preponderance of values around the mean with progressively fewer observations as the curve extends outward. The probability distribution function (PDF) used to describe the probability of the variate to belong to the group of data which have Gaussian distribution.

A multi-variate Gaussian distribution is a specific probability distribution, which can be thought of as a generalization to higher dimensions of the one-dimensional normal distribution. Skin colour distribution can be modelled by a multi-variate Gaussian joint probability density function (PDF), defined as (Terrillon *et al.*, 2000):

$$P\left(x|skin\right) = \frac{1}{\sqrt{2\pi}\sqrt{\left|\sum_s\right|}} e^{-\frac{1}{2}((x-\mu_s)^T \sum_s^{-1}(x-\mu_s))} \tag{4}$$

Here, x is a colour vector, d is the dimension of colour vector and μ_s and $\sum_s$ are the distribution parameters (Mean vector and covariance matrix, respectively). The model parameters are estimated from the training data as follow:

$$\mu_s = \frac{1}{n}\sum_{j=1}^{N} x_j \qquad \sum_s = \frac{1}{n-1}\sum_{j=1}^{N}(x_j - \mu_s)(xj - \mu_s)^T \tag{5}$$

where n is the total number of skin colour samples.

Fig. 1 shows an example of the bivariate Single Gaussian distribution, T and S represent the colure vector components and the vertical axis represents the PDF.

A particular input pixel of colour vector is classified as skin if the probability density function satisfies the following relation:

$$P\ (x|skin) \geq \Omega \tag{6}$$

where Ω here is a threshold value.
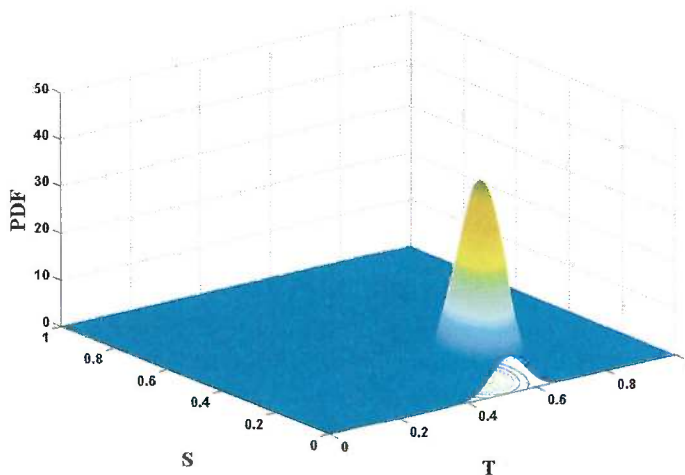
Fig. 1: Probability map of the bivariate Single Gaussian distribution

Gaussian Mixture Modeling (GMM)

A more sophisticated model, capable of describing complex-shaped distributions is the Mixture of Gaussians model (GMM). It is the generalization of the single Gaussian, the PDF in this case is:

$$P\ (x|skin) = \sum_{i=1}^{1} K_i \times P_i(x|skin) \tag{9}$$

Where l is the number of the mixture components K_i, is the mixing parameters and $P(x|skin)$ are Gaussian PDF's, each with its own mean and covariance matrix. The model training is performed with a well-known iterative technique called the Expectation Maximization (EM) algorithm, which assumes that the number of components l to be known. The choice of the components number is important. The EM algorithm is run on the training data using a stopping criterion that checks if the change in log-likelihood between the two iterations is lesser than a threshold.

Greenspan *et al.* (2001) showed that a Gaussian mixture modelling of the colour space provides a robust representation to accommodate large colour variations. They presented a face segmentation model that used a Gaussian mixture modelling with $k=2$. They demonstrated this via the GMM, and the ability to provide better overall face segmentation results, as well as the ability to analyze the different regions within a face as belonging to different colour and lighting categories is achieved.

Fig. 2 shows an example of the bivariate Gaussian Mixture distribution, T and S represent the colure vector components and the vertical axis represents the PDF.

Elliptic Boundary Modeling

By examining the skin and non-skin distributions in several colour spaces, Phung *et al.* (2005) concluded that the skin colour cluster, being approximately elliptic in shape, was not well enough approximated by the single Gaussian model. Due to the asymmetry of the skin cluster with respect to its density peak, the usage of the symmetric Gaussian
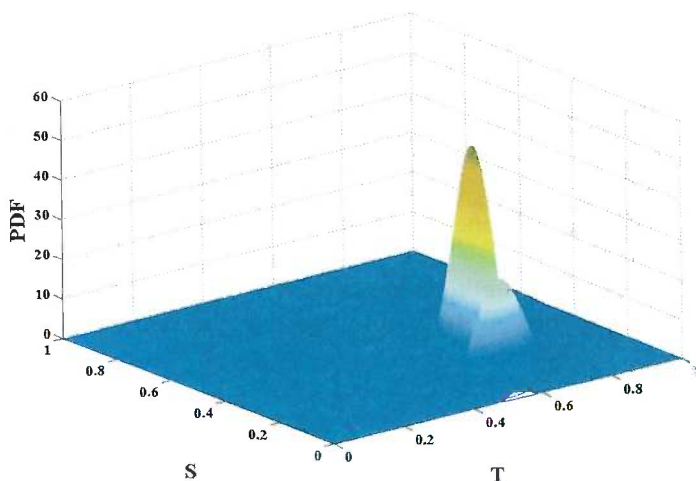
Fig. 2: Probability map of the bivariate Gaussian Mixture distribution

model leads to a high false positive rate. They proposed elliptical boundary model which is equally fast and simple in training and evaluation as the single Gaussian model.

COMPARATIVE EVALUATION FOR SKIN DETECTION METHODS

The main advantage of the methods that use explicitly defined skin cluster boundaries is the simplicity and intuitiveness of the classification rules. However, the difficulty with them is the need to find both good colorspace and adequate decision rules empirically.

The non-parametric methods are fast both in training and classification, independent to distribution shape and therefore to color space selection. However, they require much storage space and a representative training dataset. The parametric methods can also be fast, they have a useful ability to interpolate and generalize incomplete training data, they are expressed by a small number of parameters and need very little storage space. However, they can be slow (like mixture of Gaussians) in both training and work, and their performance depends strongly on the skin distribution shape. Besides, most parametric skin modeling methods ignore the non-skin color statistics.

Vezhnevets *et al.* (2003) and Phung *et al.* (2005) introduced a survey in skin detection methods. They both found that the Bayesian classifier with the histogram technique has higher classification rates compared to other tested classifiers, including piecewise linear and Gaussian classifiers. The Bayesian classifier with the histogram technique is feasible for the skin color pixel classification problem because the feature vector has a low dimension and a large training set can be collected. However, the Bayesian classifier requires significantly more memory compared to other classifiers. Parametric skin modeling methods (SGM, GMM and elliptic boundary model) are better suited for constructing classifiers in case of limited training and expected target data set. The generalization and interpolation ability of these methods makes it possible to construct a classifier with acceptable performance from incomplete training data.

CONCLUSION

From the previous review of the skin detection task, many important issues can be summarized as follows:

*   Most of the recent studies with interest in the colour spaces and its relationship with the skin detection task, state that the elimination of the luminance component in the process of skin detection doesn't improve the performance of the model. Regardless of that, most of the published research in the field of skin detection used the luminance elimination because the process of the 2D skin detection model is easier and faster, and the computation cost is lowest compared to the process of the 3D skin detection model.
*   The choice of colour space depends on the method used for modeling the skin color distribution.
*   Each of the skin detection methods has its own advantages and disadvantages, so the choice of method depends on the application that the skin detection model is to be used.

REFERENCES

Acharya, T. and Ray, A. K. (2005). *Image Processing Principles and Applications.* New Jersey: A Wiley-Interscience Publication.

Ahlberg, J. (1999). *A system for face localization and facial feature extraction.* Technical report, Report no. LiTH-ISY-R2172. Linköping, Sweden: Linköping University.

Albiolt, A., Torres, L. and Delp, E. J. (2001). Optimum color spaces for skin detection. In *Proceedings of IEEE International Conference on Image Processing (1,* 122–124). Thessaloniki, Greece.

Garcia, C., Zikos, G. and Tziritas, G. (1999). Face detection in color images using wavelet packet analysis. *IEEE International Conference on Multimedia Computing and Systems, 1,* 703-708.

Gomez, G. and Morales, E. F. (2002). Automatic feature construction and a simple rule induction algorithm for skin detection. In *Proceedings of the ICML Workshop on Machine Learning in Computer Vision* (p. 31-38). Sydney, Australia.

Greenspan, H., Goldberger, J. and Eshet, I. (2001). Mixture model for face color modeling and segmentation. *Pattern Recognition Letters, 22*(14), 1525-1536.

Jayaram, S., Schmugge, S., Shin, M. C. and Tsap, L. V. (2004). Effect of colorspace transformation, the illuminance component, and color modeling on skin detection. In *Proceedings of the 2004 IEEE Computer Society Conference on Computer Vision and Pattern Recognition (CVPR'04)* (p. 813-818). Washington, DC, USA.

Lee, J. Y. and Yoo, S. I. (2002). An elliptical boundary model for skin color detection. In *The 2002 International Conference on Imaging Science, Systems, and Technology.* Las Vegas, USA.

Peer, P., Kovac, J. and Solina, F. (2003). Human skin colour clustering for face detection. In *EUROCON 2003 - International Conference on Computer as a Tool.* Ljubljana, Slovenia.

Phung, S. L., Bouzerdoum, A. and Chai, D. (2005). Skin segmentation using color pixel classification: analysis and comparison. *IEEE Transactions on Pattern Analysis and Machine Intelligence, 27*(1), 148-154.

Terrillon, J. C., Shirazi, M. N., Fukamachi, H. and Akamatsu, S. (2000). Comparative performance of different skin chrominance models and chrominance spaces for the automatic detection of human faces in color images. In *Proceedings of the 4th IEEE International Conference on Automatic Face and Gesture Recognition* (p. 54-61). Grenoble, France.

Vezhnevets, V. and Andreeva, A. (2005). *A comparative assessment of pixel-based skin detection methods.* Technical report. Moscow, Russia: Graphics and Media Lab., Moscow State University.

Vezhnevets, V., Sazonov V. and Andreeva A. (2003). A survey on pixel-based skin color detection techniques. In *Proceedings of the Graphicon* (p. 85-92). Moscow, Russia.

Wimmer, M. and Radig, B. (2005). Adaptive skin color classificator. In *Proceedings of the first ICGST International Conference on Graphics, Vision and Image Processing GVIP-05* (p. 324-327). Cairo, Egypt.

Zarit, B.D., Super, B.J. and Quek, F.K.H. (1999). Comparison of five color models in skin pixel classification. In *Proceedings of IEEE International Workshop on Recognition, Analysis, and Tracking of Faces and Gestures in Real-Time Systems* (p. 58-63). Corfu, Greece.

Pertanika Journal of Science & Technology

Subject Index for Volume 15 Nos. 1 & 2 2007

pixel colour transformation 132
pixel-based methods 131
PMMA *see* poly(methylmethacrylate)
poly(methylmethacrylate) 121-123, 125, 127
polynomials 62-64, 74
pore water pressure 85-86, 115, 118-119
power line zone 39
power transmission lines 35-40
probability
    density function 52, 134
    distribution function 103, 105-106, 108,
       134-135

quality characteristic 50-52, 54-55
quality loss function 49-55

RBD *see* refined, bleached deodorized
Receiver Operating Characteristic 108
reception 32
recrystalization 100
refined, bleached deodorized 121
relative standard deviation 121
residual soil 85-88, 92, 113-114, 116-117
ROC *see* Receiver Operating Characteristic
Rowe cell 115-116
RSD *see* relative standard deviation

SDM see skin detection model
seventh degree form 61
SGM *see* Single Gaussia model
shear strength 113-114, 118
signal transmission 32
silica gel column 44, 78, 96
Single Gaussia model 103, 105-109, 134, 136
skin colour
    detection 103, 131-132
    distribution 103, 133-134, 136
skin detection methods 103-104, 132, 136
skin detection model 105, 108, 110

skin-segmentation algorithm 103
slope distance 38-40
soil water characteristic curve 113-114, 118-119
sonar systems 25
specification limits 49-51
spectrometer 44, 78, 96
spectrophotometer 124, 126
spectrum 44-46, 78, 80-82, 96, 99, 100
SSE *see* sum-squared error
stem bark 95
sum-squared error 124, 126-127
SWCC *see* soil water characteristic curve

target value 50-52, 54-55
temperature 1-5, 7-11
terrain, vegetation and residue 16-17, 19, 22
tetramethylsilane 44, 78
The False Positive 108-110
The True Positive 108, 110
thermal properties 1, 4, 6
thermocouple 5, 9
thermo-physical properties 6-7, 9
tint, saturation, luminance values 104-105
TMS *see* tetramethylsilane
TP *see* The True Positive
triterpenoids 43, 77
TSL *see* tint, saturation, luminance values
TVR *see* terrain, vegetation and residue
two-class classification problem 103

ULA *see* uniform linear array
uniform linear array 32

vanadium 121-122
void ratio 85, 89, 91-93, 114
volume change 85-88, 113-114
voucher specimens 95

xanthones 43, 45, 47, 77, 79, 81-82

PERTANIKA JOURNAL OF SCIENCE & TECHNOLOGY

AUTHOR INDEX FOR VOLUME 15 NOS. 1 & 2 2007

ACKNOWLEDGEMENTS